



1 **Combining Electromagnetic Induction and Remote Sensing Data for Improved**
2 **Determination of Management Zones for Sustainable Crop Production**

3

4 **Authors**

5 Salar Saeed Dogar^{1*}, Cosimo Brogi¹, Dave O’Leary^{2,3}, Ixchel Hernández-Ochoa⁴, Marco Donat^{5,6},
6 Harry Vereecken¹, and Johan Alexander Huisman¹

7 ¹ Agrosphere Institute (IBG-3), Forschungszentrum Jülich GmbH, 52425 Jülich, Germany

8 ² Hy-Res Research Group, School of Natural Sciences, Earth and Life, College of Science and Engineering, University
9 of Galway, Galway, Ireland

10 ³ Teagasc, Animal and Grassland Research and Innovation Centre, Moorepark, Fermoy, Ireland

11 ⁴ Institute of Crop Science & Resource Conservation (INRES), Crop Science Group, University of Bonn, 53115 Bonn,
12 Germany

13 ⁵ Leibniz Centre for Agricultural Landscape Research, 15374 Müncheberg, Germany

14 ⁶ Faculty of Landscape Management and Nature Conservation, University for Sustainable Development (HNEE),
15 16225, Eberswalde, Germany

16

17

18 *Corresponding Author (s.dogar@fz-juelich.de)

19

20

21

22

23

24

25



26 **Abstract**

27 Accurate delineation of management zones is essential for optimizing resource use and improving
28 yield in precision agriculture. Electromagnetic induction (EMI) provides a rapid, non-invasive
29 method to map soil variability, while the Normalized Difference Vegetation Index (NDVI)
30 obtained with remote sensing captures above-ground crop dynamics. Integrating these datasets
31 may enhance management zone delineation but presents challenges in data harmonization and
32 analysis. This study presents a workflow combining unsupervised classification (clustering) and
33 statistical validation to delineate management zones using EMI and NDVI data in a single 70 ha
34 field of the patchCROP experiment in Tempelberg, Germany. Three datasets were investigated: (1)
35 EMI maps, (2) NDVI maps, and (3) a combined EMI-NDVI dataset. Historical yield data and soil
36 samples were used to refine the clusters through statistical analysis. The results demonstrate that
37 four EMI-based zones effectively captured subsurface soil heterogeneity, while three NDVI-based
38 zones better represented yield variability. A combination of EMI and NDVI data resulted in three
39 zones that provided a balanced representation of both subsurface and above-ground variability.
40 The final EMI-NDVI derived map demonstrates the potential of integrating multi-source datasets
41 for field management. It provides actionable insights for precision agriculture, including optimized
42 fertilization, irrigation, and targeted interventions, while also serving as a valuable resource for
43 environmental modelling and soil surveying.

44



45 **1 Introduction**

46 Reliable and accurate agricultural management zones that capture within-field variability affecting
47 crop development can play a pivotal role in sustainable agriculture. Management zones can be
48 used in the context of precision agriculture to optimize farming practices, increase yields, and
49 reduce the use of available resources (Gebbers and Adamchuk, 2010; Janrao et al., 2019). This is
50 not only valuable for profit maximization (Adhikari et al., 2022), but is also vital to meet future
51 climate change and food security challenges (Antle et al., 2017; Chartzoulakis and Bertaki, 2015;
52 Bongiovanni and Lowenberg-Deboer, 2004), such as Goal 2 (Zero Hunger) and Goal 15 (Life on
53 Land) of the United Nations Sustainable Development Goals (SDGs) (Hou et al., 2020; UN, 2021).
54 Generally, management zones aim to consider the impact of various factors that can influence crop
55 productivity and result in yield gaps, a key one being soil heterogeneity and health (Licker et al.,
56 2010). Soil systems can be relatively static in time (Arshad et al., 2015) and are fundamental due
57 to their multifunctional role and impact on ecosystem services (Hamidov et al., 2018). Within these
58 systems, soil properties such as texture, organic matter content, cation exchange capacity, and bulk
59 density greatly influence soil moisture dynamics, salinity, nutrient availability, and other variables
60 affecting crop yield (Kibblewhite et al., 2008; Dobarco et al., 2021) and are thus a good target for
61 management zone delineation. However, soil heterogeneity is not solely responsible for yield
62 losses, and effective management zones should also incorporate other influencing factors to
63 provide a comprehensive and holistic management solution.

64

65 Traditional methods for soil characterization to support management zone delineation (Brogi et
66 al., 2021; NRW GD, 2025) generally rely on laborious in-situ sampling and laboratory analysis,
67 which may fail in capturing soil variability with sufficient detail (Kuang et al., 2012). In recent



68 years, advances in proximal soil sensing, defined as methods that utilize sensors positioned near
69 or in direct contact with the soil (Adamchuk et al., 2017), have provided valid alternatives to direct
70 soil sampling (Pradipta et al., 2022). In particular, non-invasive agro-geophysical methods such as
71 electromagnetic induction (EMI) have proven suitable for management zone delineation due to the
72 high mobility (Binley et al., 2015; Garré et al., 2021) and the fact that the measured apparent
73 electrical conductivity (ECa) of the soil is related to key soil properties, such as soil salinity, soil
74 water content, texture, compaction, and organic matter content (Corwin and Lesch, 2003; Abdu et
75 al., 2008; Altdorff et al., 2017; Jadoon et al., 2015; Robinet et al., 2018; Zhu et al., 2010; von Hebel
76 et al., 2018). Modern EMI devices are able to efficiently provide soil information for multiple
77 depth ranges thanks to multi-coil instrumentation (Rudolph et al., 2015; von Hebel et al., 2014;
78 Blanchy et al., 2024; Lueck and Ruehlmann, 2013; Corwin and Scudiero, 2019), especially when
79 supported by a moderate amount of ground truth data (Brogi et al., 2019). However, the use of
80 EMI alone can show limitations in capturing local aspects that have an impact on yield but that are
81 not strongly influenced by soil variability. For instance, pest and weed infestations can drastically
82 reduce crop productivity, and these factors may not correlate directly with soil variability (Becker
83 et al., 2022; López-Granados, 2011). Additionally, climate change impacts, such as altered
84 precipitation patterns and temperature fluctuations, can affect crop health and yield in ways that
85 EMI cannot detect (Pradipta et al., 2022). Finally, it is also important to stress that accurate EMI
86 mapping generally requires optimal conditions like bare soil, favourable weather, and absence of
87 confounding factors (James et al., 2003).

88

89 An alternative to proximal soil sensing for the delineation of management zones is the use of
90 remote sensing approaches, which enables efficient large-scale data acquisition without the need



91 for direct physical access to the investigated area (Weiss et al., 2020). By using sensors mounted
92 on satellites, airplanes, or drones, remote sensing monitors parameters related to crop health and
93 development (Jin et al., 2019; Liaghat and Balasundram, 2010). For example, vegetation indices
94 such as the Normalized Difference Vegetation Index (NDVI) are generally well-established,
95 simple, and effective proxies for crop health (Carfagna and Gallego, 2005; Stamford et al., 2023;
96 Wang et al., 2020; Xue and Su, 2017). High-resolution (<5 m) data products from satellites are
97 being increasingly used in precision agriculture (Mohammed et al., 2020; Trivedi et al., 2023).
98 Also, remote sensing platforms like PlanetScope, Sentinel-2, and Landsat offer frequent revisit
99 times, thus providing sufficient temporal resolution to track changes in plant health throughout the
100 growing season (Hunt et al., 2019; Skakun et al., 2021). Despite these advantages, remote sensing
101 data are affected by cloud cover or other sub-optimal meteorological conditions (Wilhelm et al.,
102 2000) and primarily capture above-ground information on plant health and biomass, and can thus
103 struggle to provide direct information about the interplay between soil conditions and crop
104 development.

105

106 Several studies have explored a combination of EMI and remote sensing methods for the
107 delineation of management zones. For example, von Hebel et al. (2021) combined EMI and drone-
108 based NDVI measurements and found that EMI-based management zones offered consistent
109 insights into soil texture and water content, while the added value of NDVI greatly varied, mostly
110 due to the timing of the drone measurements and thus on the specific crop conditions. In a similar
111 study, Esteves et al. (2022) showed that integration of EMI and NDVI from Sentinel-2 (10 m
112 resolution) effectively provided zones with distinct soil and crop nutrient characteristics. However,
113 they reported a negative relationship between EC_a and NDVI due to local magnesium imbalances



114 and vegetation stress. In addition to EMI and remote sensing, historical yield maps can help in
115 identifying yield trends across years and different cultivated crops. For example, Ali et al. (2022)
116 integrated seven years of yield data with Landsat-based NDVI and soil sampling over a 9 ha field,
117 but ultimately could obtain only a limited subdivision of the field into two management zones with
118 a relatively low resolution of 30 m. Generally, previous research highlighted that combining data
119 from different sources provides a more comprehensive assessment of above- and below-surface
120 factors affecting crop health (Corwin and Scudiero, 2019; Ciampalini et al., 2015), but a large
121 variability of the results was found across different combinations of methodologies and local field
122 conditions.

123

124 As obtaining management zones from spatial datasets based on EMI or remote sensing data can
125 be challenging, machine learning clustering algorithms have been widely used (Saifuzzaman et al.,
126 2019; Castrignanò et al., 2018; Chlingaryan et al., 2018; Zhang and Wang, 2023). For example,
127 Wang et al. (2021) used supervised Random Forest classification for combining EMI data with
128 environmental covariates to predict soil salinity. Similarly, Brogi et al. (2019) employed supervised
129 learning to combine EMI with soil sampling and generate high-resolution soil maps for a 1 km²
130 agricultural area. However, the results of supervised classification approaches may depend on the
131 interpreter and often need expert knowledge as well as extensive ground-truth data for training
132 (Liakos et al., 2018; Usama et al., 2019). K-means and ISODATA clustering are unsupervised
133 methods used to delineate management zones (Bijeesh and Narasimhamurthy, 2020; Ylagan et al.,
134 2022; Tagarakis et al., 2013) but these approaches can be sensitive to initial conditions and struggle
135 to handle non-linear relationships in datasets (Geng et al., 2020; Li et al., 2018). Thus, more
136 advanced methods such as self-organizing maps (SOM) have been successfully used to analyse



137 complicated data structures provided by proximal and remote sensing data (Romero-Ruiz et al.,
138 2024; Moshou et al., 2006; Taşdemir et al., 2012). A remaining key challenge of unsupervised
139 methods is the definition of the optimal number of clusters. Widely used approaches such as the
140 elbow and silhouette method (Saputra et al., 2020) often struggle when applied to non-linearly
141 distributed or spatially complex datasets (Schubert, 2023), and may thus require subjective
142 judgment or expert knowledge (Liang et al., 2012). To address this challenge, the Multi-Cluster
143 Average Standard Deviation (MCASD) approach that relies on an evaluation of the intra-cluster
144 variability has recently been introduced (O’Leary et al., 2023) and successfully applied to the
145 integration of complex spatial datasets (O’Leary et al., 2024). However, many of these novel
146 approaches have seen limited applications in agricultural contexts (Khan et al., 2021) and the added
147 value of delineating management zones from datasets of different origin remains unaddressed
148 (Koganti et al., 2024).

149

150 In this study, the potential of delineating management zones by integrating multi-coil EMI data
151 with satellite-based NDVI is explored for a single 70 ha agricultural field near Berlin, Germany.
152 Management zones were derived using three data sources: i) ECa maps from nine different depths
153 of investigation (DOI) obtained with EMI between 2020 and 2024, ii) seven NDVI images
154 obtained from PlanetScope in 2019, and iii) a combination of EMI and NDVI data. Management
155 zones were delineated using SOM while the optimal number of clusters was obtained with the
156 MCASD method. In a following step, the number of clusters was refined using post-hoc analysis
157 using a large dataset of soil samples and yield maps at 10 m resolution from 2011 to 2019. Finally,
158 it was evaluated to what extent management zones derived from EMI, NDVI, or a combination of
159 both represent soil characteristics and yield patterns using visual inspection and statistical analysis.



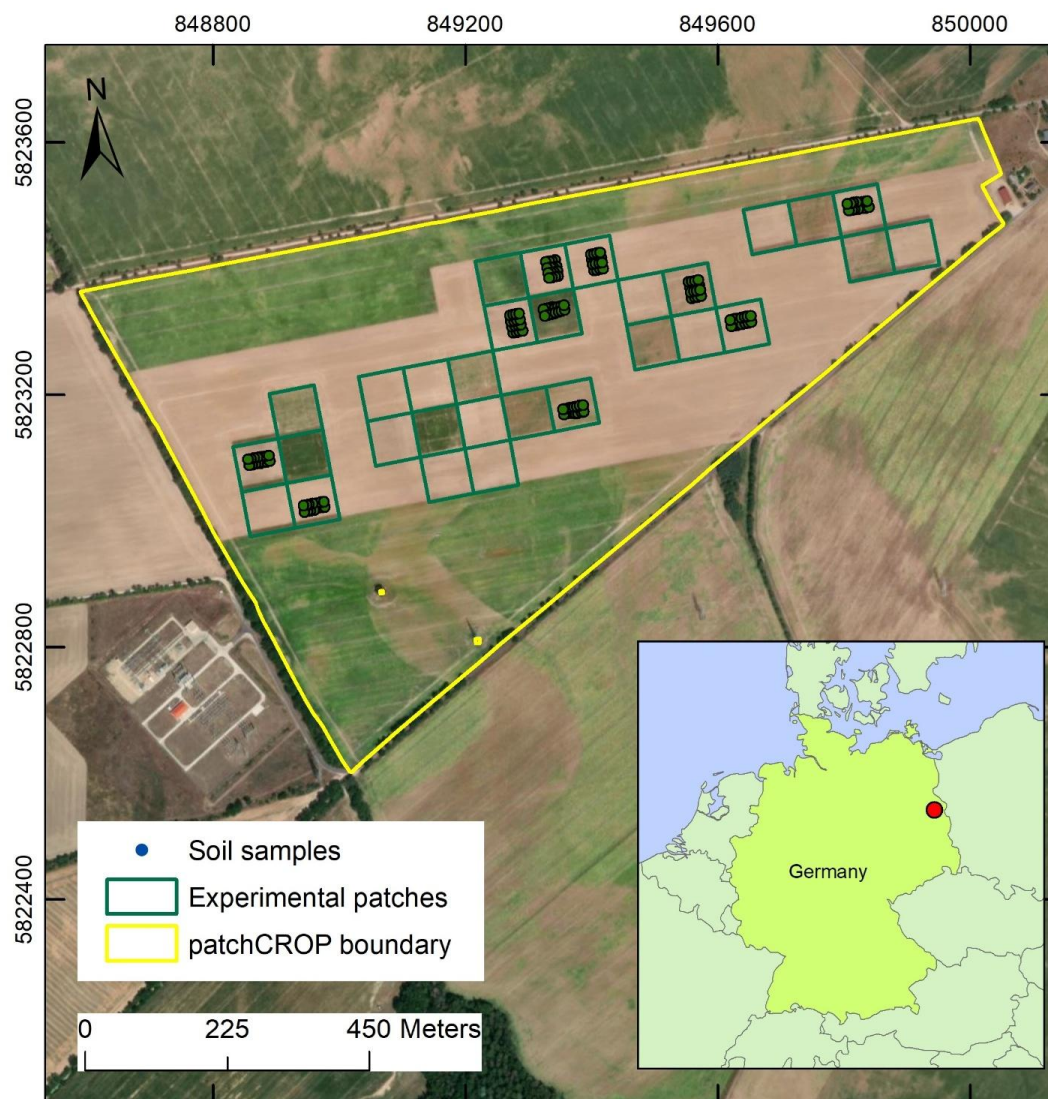
160

161 **2 Materials and Methods**

162 **2.1 Study area**

163 The study site is part of the patchCROP (patchCROP, 2020) landscape laboratory of the Leibniz
164 Centre for Agricultural Landscape Research (ZALF) near Tempelberg, Brandenburg, Germany
165 (52.4426 N, 14.1607 E, altitude 68 m). It is located in the transition zone between humid oceanic
166 and dry continental climate. The long term average temperature from 1980 to 2020 was 8.3°C and
167 the mean annual precipitation for the same period was 533 mm (DWD, 2021; Koch et al., 2023).
168 The investigated field has an area of approximately 70 ha (Fig. 1). Until 2020, this field was
169 managed as a single unit. In March 2020, the patchCROP experiment was established to study the
170 impact of landscape diversification through the use of smaller field sizes, site-specific crop
171 rotations, different field management practices, and the use of new technologies including
172 proximal soil sensing, remote sensing, and robotic technologies (Grahmann et al., 2021). For this,
173 thirty patches of 72 x 72 m were established within the investigated field (Donat et al., 2022) (Fig.
174 1). In terms of geomorphology, the site is described as a young moraine landscape shaped by past
175 glaciations, and characterized by an undulating relief and heterogeneous soil characteristics (Koch
176 et al., 2023; Öttl et al., 2021; Meyer et al., 2019). The topsoil is predominantly sandy, but a more
177 clayey layer is present at different depths in the subsoil (Hernández-Ochoa et al., 2024).

178



179

180 Figure 1. Overview of the patchCROP Study Area Tempelberg (ESRI, 2020). The yellow border
181 indicates the boundary of the investigated field, whereas the green boxes indicate the thirty patches
182 of the patchCROP landscape experiment.

183

184



185 **2.2 Data collection and processing**

186 **2.2.1 Yield data**

187 Georeferenced yield maps of nine growing seasons (2011-2019) were used. These yield maps were
188 generated using a yield monitoring system (CLAAS Quantimeter, Hersewinkel, Germany)
189 mounted on two different combine harvesters. From 2011 to 2013, data were collected using a
190 CLAAS 580. From 2014 onwards, a CLAAS Lexion 770 TT was used. In the 2011 – 2019 period,
191 the field was either cultivated with winter rye (2011, 2013, 2014, 2016, 2017, and 2019) or
192 rapeseed (2012, 2015, and 2018). For additional details on data processing and yield map
193 generation, readers are referred to Donat et al. (2022). The original yield data from Donat et al.
194 (2022) were available as georeferenced yield data points with a spacing of ~10 m. These points
195 were interpolated to a regular grid with 10 m resolution using ordinary kriging.

196

197 **2.2.2 Electromagnetic Induction (EMI) measurements**

198 Frequency-domain EMI devices generate a fixed-frequency alternating current in a transmitter
199 coil, which produces a primary magnetic field. This primary magnetic field induces eddy currents
200 in the soil, thus generating a secondary magnetic field. The primary and secondary magnetic fields
201 are sensed by a receiver coil. The quadrature component of the ratio between the primary and
202 secondary magnetic fields is directly proportional to the apparent electrical conductivity (ECa) of
203 the ground (Keller and Frischknecht, 1966; Ward and Hohmann, 1988; McNeill, 1980). The
204 measured ECa is strongly affected by soil properties such as salinity, water content, clay content
205 (and thus texture), compaction, and to a lesser degree organic matter content and cation exchange
206 capacity (Corwin and Lesch, 2005; Robinet et al., 2018). The depth sensitivity of EMI
207 measurements depends on coil spacing and coil orientation. Larger spacing results in increased



208 depths of investigation (DOI), while the coil orientation influences the sensitivity to shallow or
209 deep subsurface (Lavoué et al., 2010; Simpson et al., 2009).

210

211 In this study, two EMI devices were used simultaneously: a CMD-Mini Explorer (GF Instruments,
212 Brno, Czech Republic) with three receiver coils oriented in a vertical coplanar configuration
213 (VCP), and a custom-made CMD-Mini Explorer – Special Edition equipped with six receiver coils
214 oriented in a horizontal coplanar configuration (HCP). The VCP configuration is most sensitive to
215 the shallow subsurface, with decreasing sensitivity as depth increases. In contrast, the HCP
216 configuration is less sensitive to the shallow subsurface, with sensitivity peaking at a depth of
217 approximately 0.4 times the coil separation (McNeill, 1980). As a rule of thumb, the DOI for the
218 VCP setup is approximately 0.75 times the coil separation. For the HCP setup, the DOI is
219 approximately 1.5 times the coil separation. For the set-up used here, the resulting DOI ranges
220 from 0-24 to 0-270 cm. Details of the EMI set-up are summarized in Table 1.

221

222

223

224

225

226

227

228

229



230 Table 1. Details of the two EMI devices with coil number, orientation, separation, DOI, and
231 frequency.

| EMI device | Receivers | Orientation | Separation (cm) | DOI (cm) | Frequency (Hz) |
|-----------------|-----------|-------------|-----------------|----------|----------------|
| Mini Explorer | 3 | VCP | 32 | 0-24 | 30 |
| | | VCP | 71 | 0-53 | |
| | | VCP | 118 | 0-89 | |
| Mini Explorer | 6 | HCP | 35 | 0-52 | 25.17 |
| Special Edition | | HCP | 50 | 0-75 | |
| | | HCP | 71 | 0-108 | |
| | | HCP | 97 | 0-146 | |
| | | HCP | 135 | 0-203 | |
| | HCP | 180 | 0-270 | | |

232

233 Due to the ongoing PatchCROP experiment on small patches with variable cropping systems, it
234 was not possible to cover the entire field in a single EMI campaign. EMI data were thus collected
235 in four campaigns conducted between August 2022 and October 2024. During each campaign, the
236 EMI devices were placed in sleds and warmed up for approximately 30 minutes before use. The
237 sleds were then pulled by an all-terrain vehicle (ATV) at a speed of approximately 6 to 8 km/h.
238 Data collection occurred at a frequency of 0.2 s, resulting in an inline spatial resolution of 0.25 to
239 0.50 m. A track spacing of ~2.5 m was used within the experimental patches and a track spacing
240 between 5 to 45 m (typically well below 10 m) was used in the rest of the field. A Real Time
241 eXtended (RTX) center point differential global positioning system (DGPS) (Trimble Inc.,
242 Sunnyvale, United States) was used to record the position of the sleds with centimeter accuracy.



243 For more information about the setup for EMI measurements, the reader is referred to von Hebel
244 et al. (2018).

245

246 The measured ECa values were filtered using a Python-based method similar to the approach of
247 von Hebel et al. (2014), which has been successfully applied in several studies (Brogi et al., 2019;
248 Kaufmann et al., 2020; Schmäck et al., 2022; von Hebel et al., 2021). The first filter removes
249 values that are deemed too high or too low based on user-defined thresholds (-50 and 50 mS/m in
250 this study). A second filter divides the data into a user-defined number of bins (20 in this study)
251 and removes the data from bins with a low fraction of measurements (<1% in this study). In a third
252 step, a spatial filter is used to identify and discard ECa values that deviate from adjacent positions
253 more than a given amount (1 mS/m in this study) to avoid unrealistically high lateral ECa
254 variations. After the application of these three filters, ~5% of the measured ECa values were
255 removed although this value varied between measurement campaigns.

256

257 Given that the EMI data were acquired in four campaigns with different environmental conditions
258 (e.g. soil water content, soil temperature), each EMI acquisition campaign was separately
259 normalized by using a standardized z-score normalization method as used by Rudolph et al. (2015):

260

$$261 \quad ECa_{z,i} = (ECa_i - \mu_i) / \sigma_i \quad (1)$$

262

263 where $ECa_{z,i}$ is the normalized ECa value for the i-th campaign, ECa_i is the measured ECa value
264 for the i-th campaign, μ_i is the mean ECa value of the i-th campaign, and σ_i is standard deviation
265 of ECa values for the i-th campaign. Following normalization, manual cleaning was conducted in



266 ArcMap v10.8.2 (ESRI, Redlands CA, USA) to remove points typically occurring at the start and
267 end of each campaign or in short periods where the EMI system was left stationary. In the final
268 step, the normalized data for each of the nine coil configurations were interpolated to a regular 3
269 by 3 m grid using ordinary Kriging with a gaussian semivariogram and merged into a single
270 multidimensional raster mosaic dataset.

271

272 **2.2.3 Remotely sensed NDVI data**

273 High-resolution PlanetScope Level 3B satellite images from the 2019 growing season (winter rye)
274 were used to obtain NDVI maps. Between 01/01/2019 and 31/07/2019, 48 cloud free images were
275 available. Seven of these images were selected to represent crop development during the growing
276 season. PlanetScope image products are pre-processed and have already undergone radiometric
277 and atmospheric corrections. No additional pre-processing was required. The PlanetScope sensor
278 captures spectral information in four bands: blue (B1), green (B2), red (B3), and near-infrared
279 (NIR - B4) with a spatial resolution of 3 m. The normalized difference vegetation index (*NDVI*)
280 was calculated using the reflectance in the red (*R*) and near-infrared bands (*NIR*):

281

$$282 \quad NDVI = (NIR - R)/(NIR + R) \quad (2)$$

283

284 The resulting NDVI values range from -1 to 1, where values close to 1 indicate healthy vegetation,
285 and values close to zero or negative values generally represent non-vegetated surfaces, senescent,
286 stressed or unhealthy plants or dry vegetation, or features such as clouds and water that exhibit
287 lower NIR reflectance (Wasonga et al., 2021).

288



289 **2.2.4 Soil sampling and data on soil characteristics**

290 Extensive soil sampling campaigns were conducted between 2020 and 2024, focusing on the
291 experimental patches within the 70 ha field. At 160 locations, soil samples up to 100 cm depth
292 were obtained using a Pürckhauer soil auger with an 18 mm inner diameter. The soil properties
293 analyzed in this study included the depth of soil texture transition, defined as the depth (in cm) at
294 which the sandy top layer ends (EOS layer (end of sandy layer) in the following), as well as the
295 soil texture (percentages of sand, silt, and clay) of the top sandy layer and the layer below. Soil
296 texture was determined by using the wet sieving and sedimentation method (ISO, 2002). The
297 particle size distribution was defined according to the IUSS Working Group 150 WRB guidelines
298 (IUSS Working Group, 2015). When multiple subsamples for a single layer were available at a
299 given location, weighted averages of sand, silt, and clay fraction for the whole layer were obtained
300 using the thickness of each subsample.

301

302 **2.3 Clustering for delineation of management zones**

303 Three different data combinations were created and investigated: a) EMI maps, b) time-series of
304 NDVI maps, and c) a combination of the EMI maps and NDVI maps. Before clustering, a standard
305 preprocessing step of normalization was applied on each dataset to ensure that variables with
306 different ranges and units contribute equally in the classification process. The choice of
307 normalization method can be particularly important when combining datasets with different scales,
308 such as EMI and NDVI, to prevent dominance of one dataset over the other and to maintain the
309 integrity of the input features In this study, a min-max scaling was applied, where all values were
310 rescaled to a standard range between 0 and 1 (Patro and Sahu, 2015).

311



312 For EMI, a single normalization was applied to the nine Ea_z maps. In this case, the min-max
313 normalization used the minimum ($Ea_{z\ min}$) and maximum value ($Ea_{z\ max}$) from all nine 9 maps:
314

$$315 \quad E'_{a_z} = \frac{Ea_z - Ea_{z\ min}}{Ea_{z\ max} - Ea_{z\ min}} \quad (3)$$

316
317 where Ea_z is the original value, and E'_{a_z} is the normalized value. For NDVI, each of the seven
318 NDVI maps was normalized independently:

$$319 \quad NDVI'_i = \frac{NDVI_i - NDVI_{i\ min}}{NDVI_{i\ max} - NDVI_{i\ min}} \quad (4)$$

321
322 where $NDVI'_i$ is the normalized value for the i-th map, $NDVI_i$ is the original value of NDVI of the
323 i-th map, $NDVI_{i\ min}$ and $NDVI_{i\ max}$ are the minimum and maximum values of the i-th NDVI map.
324 This difference in normalization was necessary to preserve the depth-dependent structure of EMI
325 data, as Ea represents a bulk measurement where each reading is influenced by adjacent depths.
326 In contrast, NDVI measurements are independent and acquired at different time points, and thus
327 reflect temporal variations in vegetation dynamics.

328
329 In this study, a Self-Organizing Map (SOM), an unsupervised machine learning classification
330 technique, was used for clustering (Kohonen, 2013). SOM is a centroid-based clustering technique,
331 similar in some aspects to K-means clustering (Celebi et al., 2013). While K-means clustering
332 assigns each data point to a cluster based on the minimum distance to the cluster centroid in the
333 data space, SOM utilizes an artificial neural network to organize and visualize high-dimensional
334 data (Valentine and Kalnins, 2016). The key distinction lies in how SOM projects the data onto a



335 two-dimensional grid while preserving the topological relationships of the input data. Each data
336 vector in SOM is assigned to a numerical cluster, where the cluster centre is representative of all
337 the data points associated with it. These cluster centres, which have dimensions similar to the input
338 data vectors, adjust iteratively during the training process to better represent the underlying data
339 distribution. This approach allows SOM to effectively map complex data patterns while
340 maintaining the spatial relationships between clusters.

341

342 The Multi-Cluster Average Standard Deviation (MCASD) approach was used to determine the
343 optimal number of clusters for SOM. This method evaluates the stability of the cluster centres in
344 the dataspace over multiple clustering attempts as the number of clusters increases. This metric
345 assumes that an appropriate number of clusters for a dataset is any at which the cluster centres do
346 not vary significantly when the clustering algorithm is run multiple times. In this study, MCASD
347 analysis was tested with a maximum number of 20 clusters with 100 SOM clustering runs for each
348 number of clusters to calculate the MCASD stability metric. Upon completion of MCASD
349 analysis, the highest number of clusters with a low MCASD metric is selected, as this represents
350 the maximum resolution of the spatial variability that can be obtained through clustering (O’Leary
351 et al., 2023). This clustering process was performed in MATLAB v2023a (MathWorks, Natick,
352 Massachusetts, USA).

353

354 **2.4 Statistical analysis**

355 To assess the differences between clusters derived from the three datasets, a one-way analysis of
356 variance (ANOVA) was conducted in SPSS (IBM, Chicago, IL, United States). This ANOVA
357 analysis was used to identify whether there were significant differences between clusters in terms



358 of soil properties or yield using a significance threshold of $p < 0.05$. Following the ANOVA, a
359 Tukey's HSD (Honestly Significant Difference) test was used as a post-hoc analysis to determine
360 which of the clusters were significantly different. In this step, the depth of the sandy layer, the
361 texture of the overlying layer, the texture of the layer below, and the yield data were used. Thus,
362 this step is complimentary to the previous cluster selection step with MCASD, which did not
363 consider soil and yield data. Clusters that did not exhibit significant differences were merged
364 during a reclassification step, refining the clustering results to ensure that each final cluster was
365 distinct and statistically meaningful, both in terms of the input datasets and in terms of soil
366 properties and yield. The latter was confirmed using two tailed t-test between matching layers of
367 adjacent soil classes in the reclassified map.

368

369 **3 Results and Discussion**

370 **3.1 Yield, ECa_z , and NDVI maps**

371 The yield, ECa_z , and NDVI maps highlight unique aspects of field heterogeneity and offer insights
372 into subsurface soil properties, above-ground crop performance, and their combined effects on
373 productivity. In the following, these input datasets for management zone delineation are briefly
374 introduced.

375

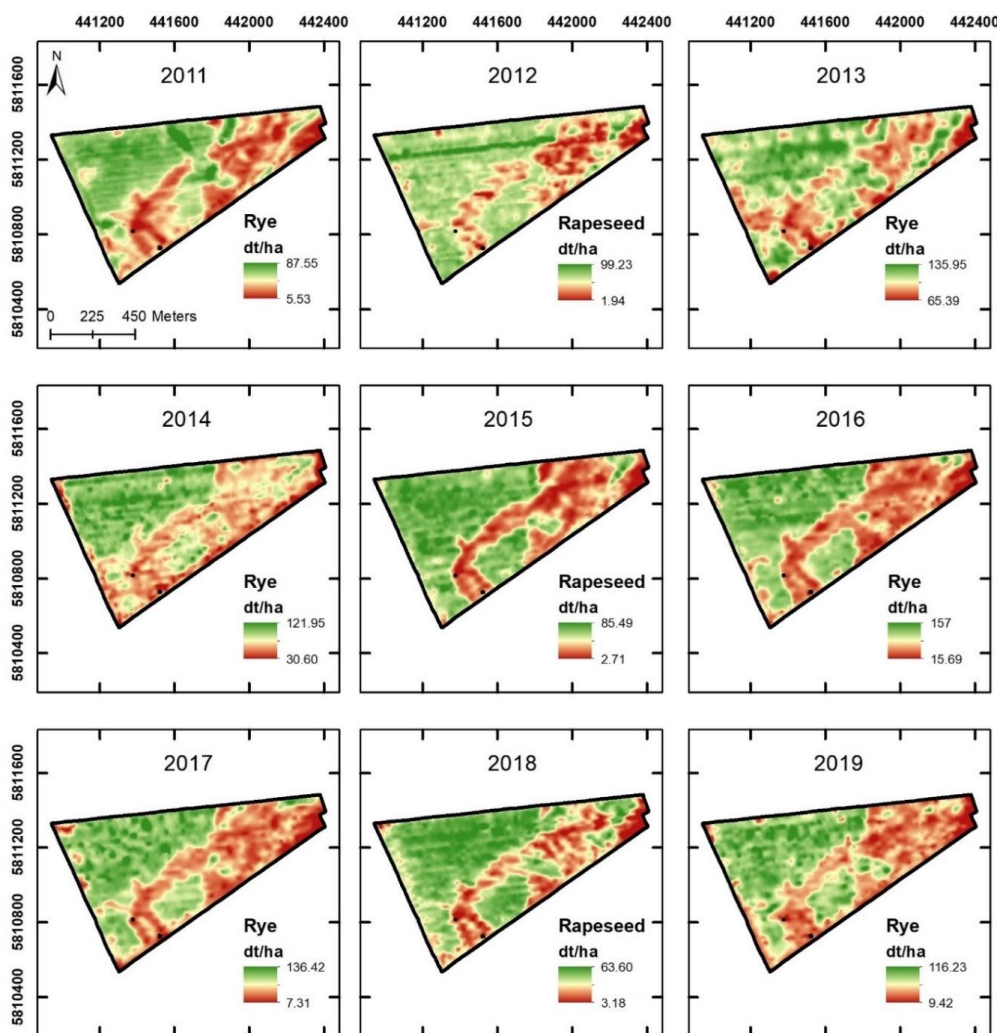
376 **3.1.1 Yield maps**

377 Figure 2 presents nine years (2011–2019) of yield maps interpolated at a 10 m resolution to
378 represent spatial variability across the field. The maps illustrate distinct patterns of high and low
379 productivity areas. Yield variability is consistent across multiple years, although variations in
380 measured yield can be observed between years. The years 2012 and 2013 show lower quality yield



381 data due to incomplete datasets (Donat et al., 2022) caused by equipment issues and environmental
382 challenges during data collection. Despite these limitations, the maps successfully capture the
383 general spatial yield trends and heterogeneity of the field. The high and low yield zones align with
384 known intrinsic field characteristics, such as soil texture, moisture retention, and nutrient
385 availability (Grahmann et al., 2024). These yield patterns will serve as validation for comparing
386 the management zones derived from EMI and NDVI data, as both datasets aim to explain the
387 variability in productivity.

388



389

390 Figure 2: Nine interpolated yield maps (2011–2019) for the patchCROP field showing spatial
391 variability of crop yield at a 10 m resolution. The maps illustrate yield distributions for winter rye
392 (2011, 2013, 2014, 2016, 2017, 2019) and rapeseed (2012, 2015, 2018). High-yield areas (green)
393 and low-yield areas (red) reflect the inherent field heterogeneity. Variability is observed both
394 within and across years, influenced by crop type, management practices, and environmental
395 conditions. The yield range for each year is provided in decitonnes per hectare (dt/ha).

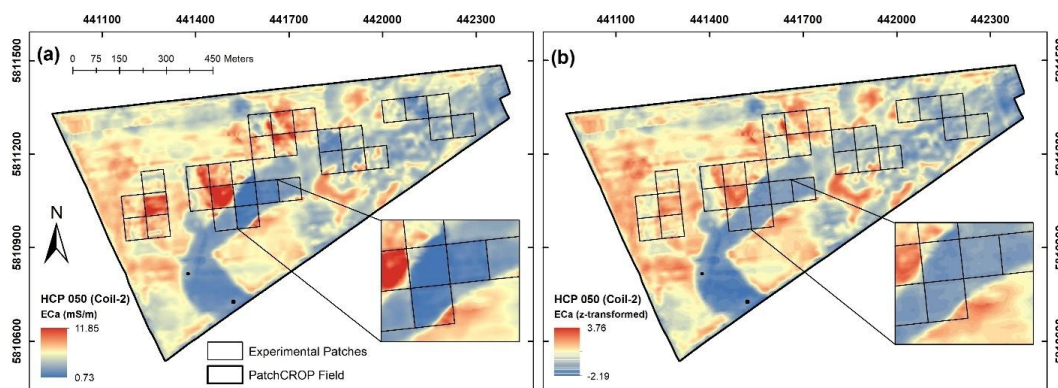


396

397 **3.1.2 EMI maps**

398 Nine ECa maps with 3 m resolution were obtained from the interpolation of the nine coil
399 configurations recorded during the EMI measurements. The results for one coil configuration
400 (HCP 050 cm) are exemplary shown in Fig. 3 before and after normalization. The study area was
401 measured under varying conditions in terms of soil temperature, soil moisture, and effect of
402 agricultural management. This resulted in differences of average ECa and spatial patterns (Fig.
403 3a). Although it is known that temperature affects measured ECa (Pedrera-Parrilla et al., 2016;
404 Vogel et al., 2019), it was not possible to perform a comprehensive temperature correction in this
405 study due to the lack of sufficient soil temperature data. Moreover, it has been shown that
406 temperature correction has limitations compared to normalization methods when the dataset is
407 composed of various depths of investigation and is affected by multiple agricultural management
408 practices (Brogi et al., 2019; Rudolph et al., 2015). Thus, Z-score normalization was applied for
409 each measurement campaign to reduce the differences between data measured on different days.
410 Figure 3b shows the normalized EMI map for the same coil configuration as shown in Fig. 3a. The
411 normalization successfully harmonized the data, minimizing the influence of varying soil moisture
412 and temperature during acquisition, resulting in more consistent spatial patterns that better
413 represent subsurface soil properties. However, some localized artefacts in the normalized maps
414 still persist. For example, areas near the field boundaries or experimental patches exhibit subtle
415 inconsistencies that may be influenced by edge effects or localized disturbances. Despite these
416 minor limitations, the normalized ECa maps provide a robust foundation for further analysis and
417 management zone delineation.

418



419

420 Figure 3. Comparison of apparent electrical conductivity (Eca) maps before and after z-score
421 normalization for the HCP 050 configuration with (a) the non-normalized Eca map, where the
422 zoomed-in section highlights the influence of varying environmental conditions such as soil
423 moisture and temperature leading to inconsistent patterns and (b) the z-score normalized Eca map,
424 which minimizes the influence of these external factors.

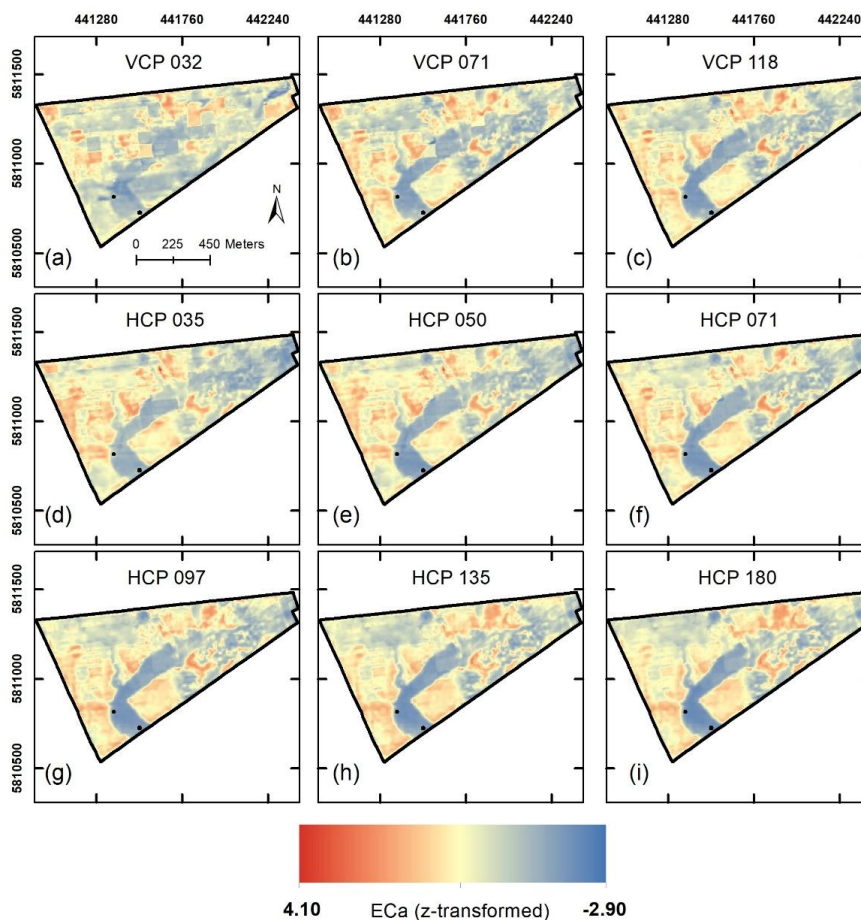
425

426 Figure 4 shows the nine normalized EC_{a_z} maps for the VCP and HCP configurations. These maps
427 display heterogeneous patterns of EC_{a_z} , primarily attributed to variations in soil characteristics in
428 space and with depth. A prominent feature is the elongated channel extending from the northeast
429 to the southwest of the field, which represents areas with lower EC_{a_z} values. This feature is
430 associated with sandy soils that generally hold less water and nutrients, indicating a coarse-
431 textured zone with lower electrical conductivity. In contrast, the northwest and southeast regions
432 of the field exhibit medium to high EC_{a_z} values, which may reflect areas of higher moisture content
433 and finer soil particles, such as loamy textures. Additionally, in the northeastern part of the field,
434 a more heterogeneous area with short-scale variations can be observed where the EC_{a_z} values vary
435 considerably between the nine maps. For the shallow VCP configurations, this area shows low



436 ECa_z values, which are indicative of sandy soils or dry conditions near the surface. For the deeper
437 HCP configurations, this same area shows higher ECa_z values, suggesting an increase in soil
438 moisture or finer soil texture at greater depths. This pattern highlights the layered soil
439 heterogeneity in this region, with subsurface properties differing significantly from the surface.
440 Overall, the EMI data reveal a high degree of spatial variability and provide valuable insights into
441 subsurface soil variability, which is critical for precision agricultural management.

442



443

444 Figure 4. Normalized apparent electrical conductivity (ECa_z) maps derived from electromagnetic
445 induction (EMI) measurements using multiple coil separations in vertical coplanar (VCP) and
446 horizontal coplanar (HCP) configurations. These maps highlight the spatial variability of
447 subsurface soil properties, with higher ECa_z values (red) indicating areas of higher moisture
448 retention or finer soil textures, and lower ECa_z values (blue) corresponding to sandy soils with
449 lower conductivity.

450



451 **3.1.3 NDVI maps**

452 All available PlanetScope satellite images for the growing season 2019 (winter rye) were visually
453 evaluated to assess their usability. Before April 2019, no meaningful patterns in NDVI were
454 observed due to the relatively short height (10 to 20 cm) and low biomass of winter rye and the
455 lack of water- or nutrient-induced stress in this early growth stage. Moreover, images from July
456 2019 were excluded from the analysis as the crop had reached maturity, and no further growth or
457 development was evident. By this time, the physiological activity of the plants had ceased, and
458 harvesting was completed on 04 August 2019.

459

460 After this initial analysis, seven NDVI images spanning the period between April and June, hence
461 from flowering to maturity, were selected for further analysis. The descriptive statistics of the
462 NDVI data are given in Table 2 and show a high degree of temporal variation. The NDVI maps
463 shown in Fig. 5 strongly resemble those of the yield maps, especially towards the end of the
464 growing season. Following crop development during the growing season, the mean NDVI peaked
465 on 30 April 2019 (221 days after sowing). Afterwards, NDVI values gradually declined as the crop
466 approached maturity, which is consistent with physiological changes during growth of winter rye
467 (Hatfield and Prueger, 2010). Figure 5 also illustrates the temporal development of the spatial
468 variation of NDVI, again pointing to the spatial heterogeneity of crop performance within the field
469 (especially Figure 5d-g) where areas of lower NDVI are associated with poorer crop performance
470 and areas of higher NDVI indicate healthier crops. Generally, the key patterns in crop performance
471 are in good agreement with the patterns observed in the EMI maps. Areas with persistently low
472 NDVI values generally correspond to areas with low ECa_z , and areas with high NDVI values
473 mostly correspond to areas with high ECa_z . However, differences between patterns in NDVI and
474 EMI can also be found. This is expected given that the dynamic changes in crop vigour and



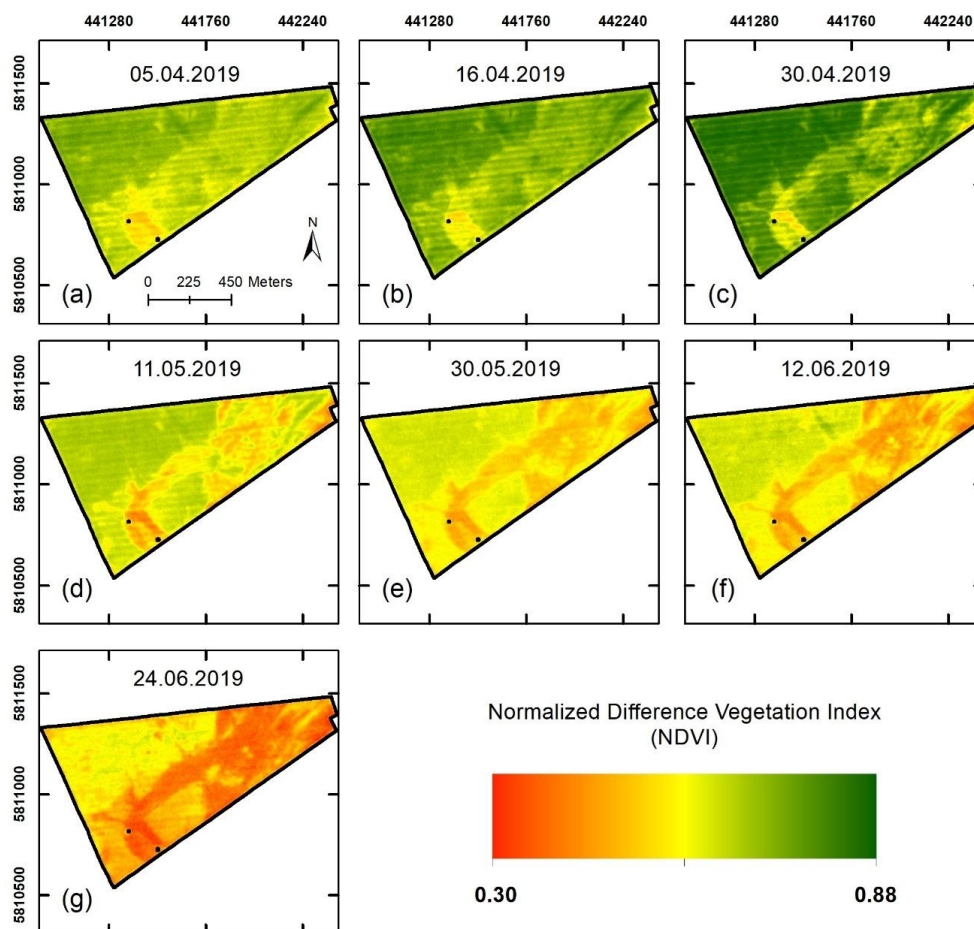
475 vegetation health shown by NDVI are not solely related to subsurface soil conditions captured by
476 EMI. For example, specific areas with low NDVI values were observed in regions of medium to
477 high ECa_z , possibly reflecting localized crop stress due to non-soil-related factors such as disease,
478 waterlogging, or nutrient imbalances.

479

480 Table 2. Summary of remotely sensed NDVI imagery and corresponding dates after sowing.

| Date of acquisition | Days after sowing | Mean NDVI | Max NDVI | Min NDVI |
|----------------------------|--------------------------|------------------|-----------------|-----------------|
| 05 April 2019 | 196 | 0.67 | 0.78 | 0.42 |
| 16 April 2019 | 207 | 0.72 | 0.85 | 0.46 |
| 30 April 2019 | 221 | 0.76 | 0.88 | 0.38 |
| 11 May 2019 | 232 | 0.61 | 0.71 | 0.34 |
| 30 May 2019 | 251 | 0.58 | 0.66 | 0.41 |
| 12 June 2019 | 263 | 0.49 | 0.65 | 0.31 |
| 24 June 2019 | 276 | 0.49 | 0.71 | 0.30 |

481



482

483 Figure 5. Seven NDVI maps derived from PlanetScope satellite imagery representing the temporal
484 variability in vegetation development during the 2019 growing season. The images, dated from
485 05/04/2019 to 24/06/2019, capture critical crop growth stages, including flowering and maturity.

486

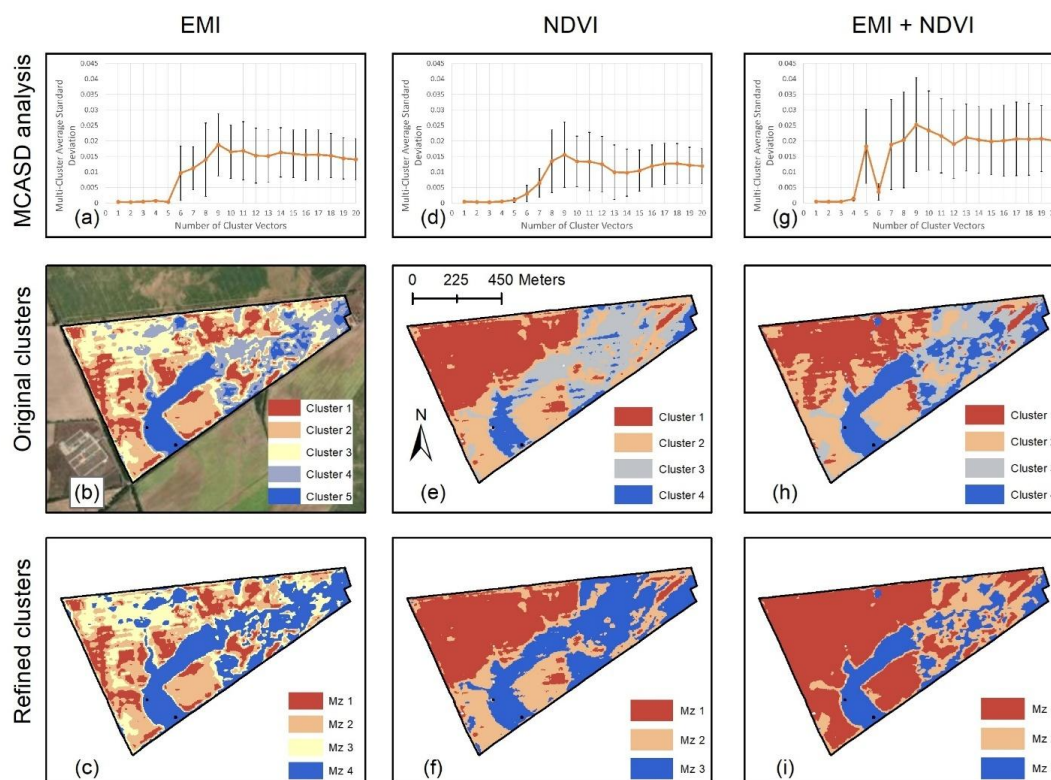
487 3.2 Clustering of EMI and NDVI

488 The MCASD analysis for the three datasets provided a robust method to determine the optimal
489 number of clusters (Fig. 6). The analysis suggested a maximum of five clusters for the EMI data
490 (Fig. 6b). These clusters reflect differences in subsurface properties such as soil texture, moisture,



491 and compaction. Cluster 1 corresponds to areas with the highest E_{Ca_z} values, which gradually
492 decrease with each subsequent cluster. Cluster 5 represents the lowest E_{Ca_z} values. For NDVI (Fig.
493 6e), a maximum of four clusters was selected. While a five-cluster solution was initially identified
494 as viable for NDVI, increasing the number of clusters beyond four did not significantly reduce
495 variability. This made the four-cluster solution more practical and efficient for representing spatial
496 variability in the NDVI data. Cluster 1 identifies areas with relatively high NDVI values, indicative
497 of healthy, dense vegetation and higher crop performance. NDVI values progressively decrease
498 with higher cluster numbers, with cluster 4 showing the lowest values, representing stressed or less
499 productive areas. The combined EMI and NDVI dataset resulted in four clusters (Fig. 6h). Visual
500 inspection suggests that both the EMI- and NDVI-based patterns are preserved in the combined
501 dataset, likely due to the min-max scaling applied to standardize each dataset before MCASD
502 analysis (see Appendix A). Clusters 1 and 2 represent areas with high values for both E_{Ca_z} and
503 NDVI, while cluster 4 identifies zones with low values for both variables, integrating both above-
504 ground and subsurface variability effectively.

505



506

507 Figure 6. Clustering results for the PatchCROP experimental site. **(a)** MCASD analysis showing
508 appropriate cluster numbers for EMI data. **(b)** Spatial distribution of original EMI clusters (ESRI,
509 2020). **(c)** Spatial distribution of refined EMI clusters after post-hoc analysis. **(d)** MCASD analysis
510 for NDVI data. **(e)** Spatial distribution of original NDVI clusters. **(f)** Spatial distribution of refined
511 NDVI clusters after post-hoc analysis. **(g)** MCASD analysis for the combined (EMI + NDVI)
512 dataset. **(h)** Spatial distribution of the original clusters based on the EMI and NDVI data. **(i)** Spatial
513 distribution of the refined clusters for the combined dataset after post-hoc analysis.

514

515

516



517 3.3 Post-Hoc analysis

518 Starting from the optimal number of clusters identified with MCASD, a post-hoc analysis based
519 on the nine available yield maps and the point-scale soil samples was conducted. The aim was to
520 verify that the cluster are not only statistically separated in terms of the input data (i.e., EMI, NDVI
521 or a combination of EMI and NDVI), but also in terms of yield and soil characteristics (i.e., texture
522 of the first and second layers, depth to the second layer). For the EMI-based clusters, 18 soil
523 sampling locations were within Cluster 4 and only four of these had an EOS layer within 100 cm
524 depth. The other 14 locations had EOS layer below the sampling depth of 100 cm and thus no
525 textural values for the lower layer. Thus, the EOS layer depth of Cluster 4 was assumed to be below
526 100 cm and the texture of the lower layer was excluded from further analysis to have a more
527 consistent characterization of the prevailing soil characteristics.

528

529 Post-hoc analysis indicated that not all clusters were significantly different from each other, either
530 in terms of yield or soil characteristics, for all three datasets. Based on the results of the post-hoc
531 analysis, clusters were either left separated when yield or soil characteristics were statistically
532 different ($p < 0.05$) or grouped together when no statistical separation was identified. For example,
533 in the EMI-based clusters, Clusters 1, 2, and 3 had at least one significant difference in texture,
534 EOS layer, or yield. On the contrary, cluster 4 and 5 did not show statistically significant
535 differences. Thus, Cluster 4 and 5 were merged together and the resulting EMI-based cluster map
536 had four clusters with statistically significant separation of input data (i.e., EMI), yield, and soil
537 characteristics. A more detailed breakdown of this post-hoc analysis and the resulting merging
538 decisions is provided in Appendix B.

539



540 The resulting refined maps (Fig. 6c, f and i) now have clusters that are statistically separated in
541 terms of the input dataset (i.e., EMI and NDVI) but also in terms of the target variables, which are
542 yield and soil characteristics. Therefore, they are referred to as management zones instead of
543 clusters from this point onwards. These management zones maps appear to be a simplification of
544 the original clustered maps (Fig. 6b, e and h), but they now provide a more holistic understanding
545 of the field by integrating below-ground (EMI) and above-ground (NDVI) information with yield
546 and soil data.

547

548 **3.4 Assessment of management zones derived from different datasets**

549 For each management zone of the maps derived from EMI, NDVI, and a combination of EMI-
550 NDVI, Table 3 shows the average yield between 2011 and 2019 and average soil characteristics,
551 specifically the depth of soil texture transition EOS, and the textural fractions (percentages of sand,
552 silt, and clay) of two layers up to 100 cm depth. The average yields of Table 3 vary considerably
553 between different years and follow a general trend of decreasing yields with increasing cluster
554 number. Thus, yields decrease with decreasing EC_{a_z} and NDVI.

555

556

557

558

559



560 Table 3. Average values of yield (dt/ha) and soil properties for the management zones (MZs)
 561 derived from EMI, NDVI, and a combination of EMI and NDVI.

| | | EMI | | | | NDVI | | | EMI-NDVI | | | |
|-----------------------------|--------------------------------|-----------------------|-------|-------|------|-------|-------|-------|----------|------|------|------|
| | | MZs | 1 | 2 | 3 | 4 | 1 | 2 | 3 | 1 | 2 | 3 |
| Yield | 2011 | 49.5 | 44.7 | 46.5 | 31.7 | 55.9 | 41.1 | 27.5 | 50.7 | 33.1 | 25.7 | |
| | 2012 | 53.4 | 53.1 | 52.6 | 38 | 57.9 | 52.2 | 34.4 | 56.2 | 41.2 | 32.6 | |
| | 2013 | 106.3 | 105.6 | 106.5 | 98.1 | 111.1 | 104.9 | 94.49 | 108.8 | 99.1 | 93.4 | |
| | 2014 | 86.4 | 83.9 | 86.3 | 72.5 | 95.3 | 78.5 | 69.0 | 89.3 | 72.5 | 67.8 | |
| | 2015 | 55.1 | 53.7 | 51.0 | 28.5 | 62.9 | 50.1 | 22.2 | 59.1 | 31.1 | 20.5 | |
| | 2016 | 94.0 | 93.1 | 90.2 | 62.3 | 108.5 | 85.2 | 53.4 | 101 | 61.4 | 53.0 | |
| | 2017 | 78.7 | 76.0 | 73.7 | 47.9 | 89.4 | 69.4 | 41.0 | 83.3 | 48.5 | 39.5 | |
| | 2018 | 40.3 | 39.6 | 38.8 | 26.9 | 44.8 | 37.6 | 23.7 | 42.6 | 29.0 | 21.9 | |
| | 2019 | 71.0 | 69.1 | 67.2 | 48.1 | 80.2 | 62.5 | 43.1 | 74.6 | 47.7 | 42.2 | |
| Soil characteristics | Layer 1 (above EOS) | Sand % | 68.2 | 72.4 | 78.1 | 86.2 | 68.6 | 79.5 | 87.2 | 69.8 | 88.4 | 85.2 |
| | | Silt % | 23.3 | 20.0 | 16.1 | 9.6 | 23.0 | 15.2 | 8.9 | 22.2 | 8.1 | 10.4 |
| | | Clay % | 8.5 | 6.9 | 5.7 | 4.1 | 8.0 | 5.2 | 3.8 | 7.7 | 3.4 | 4.3 |
| | | Depth (cm) | 54.0 | 66.9 | 73.1 | 100 | 62.7 | 71.0 | 87.4 | 63.8 | 77.0 | 100 |
| | Layer 2 (below EOS) | Sand % | 58.3 | 58.0 | 60.6 | NA | 58.1 | 57.8 | 66.1 | 58.1 | 64.9 | NA |
| | | Silt % | 23.0 | 23.2 | 21.9 | NA | 23.1 | 23.1 | 19.3 | 23.1 | 19.9 | NA |
| | | Clay % | 18.6 | 18.7 | 17.5 | NA | 18.7 | 19.0 | 14.5 | 18.8 | 15.1 | NA |

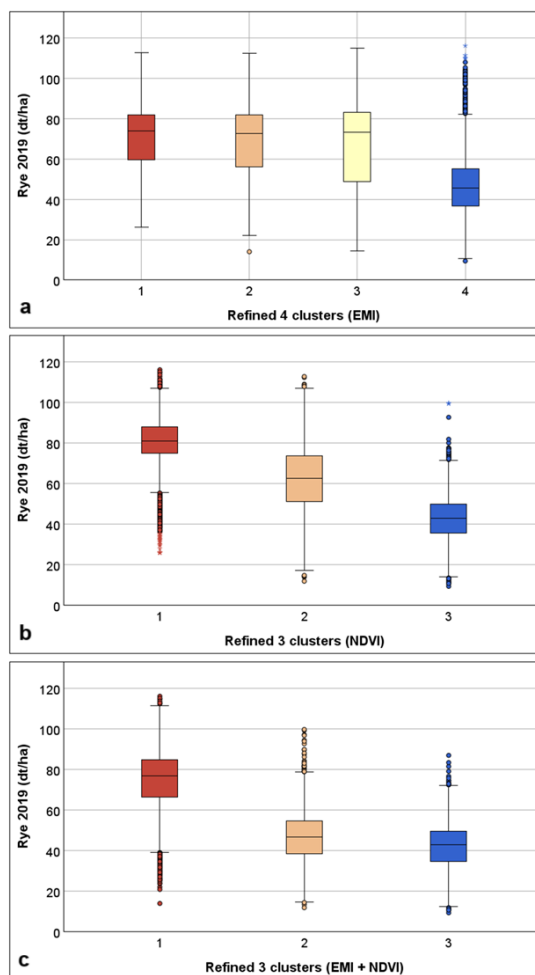
562

563 Figure 7 shows the variation in rye yield (dt/ha) for the management zones derived from different
 564 data sources for the year 2019, which is considered representative for most previous years while
 565 also allowing a direct comparison with the NDVI data for the 2019 growing season. For the EMI-
 566 based management zones (Fig. 7a), the yield distributions for the zones 1-3 are relatively similar,
 567 with overlapping interquartile ranges and medians. This indicates that, in the investigated area,
 568 EMI-based management zones are more reflective of subsurface soil properties than yield



569 variability. However, zone 4 showed significantly lower yields, corresponding to sandy soils with
570 poor moisture retention (see Table 3). The NDVI-based management zones (Fig. 7b) demonstrate
571 stronger differentiation in yield distribution and a more consistent decline in yield between zones,
572 reflecting the ability of NDVI to capture above-ground vegetation vigour and crop health. In
573 particular, zone 2 reflects an intermediate yield zone between zone 1 and 3, showcasing the ability
574 of NDVI to differentiate changes in crop performance. The management zones derived from
575 combining EMI and NDVI (Fig. 7c) offer narrower interquartile ranges, particularly in zone 2,
576 compared to NDVI-based management zones. This indicates that the integration of EMI and NDVI
577 provides a more consistent and stable representation of yield variability, combining subsurface soil
578 properties with above-ground dynamics. Although NDVI alone offers slightly more pronounced
579 yield differentiation, the combined dataset balances both subsurface and vegetation-related factors
580 effectively, making it a robust approach for management zone delineation. Similar boxplots for
581 additional years are provided in Appendix C.

582



583

584 Figure 7. Boxplots illustrating rye yield (dt/ha) for 2019 across management zones (MZs)

585 derived from (a) EMI, (b) NDVI, and (c) a combination of EMI and NDVI datasets.

586

587 The refined management zones can be associated with a typical soil profile based on the average

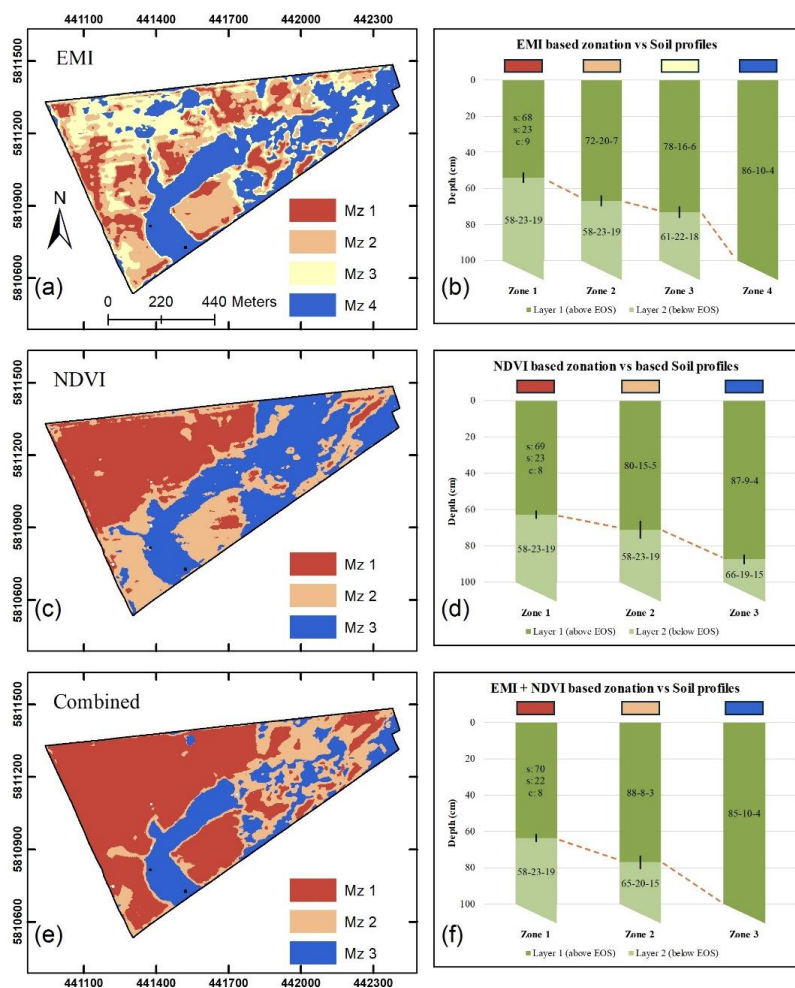
588 soil characteristics (Fig. 8). The soil profiles show the textural properties of the first two soil layers

589 and the depth of the interface between these layers (EOS) up to a depth of 100 cm. In some profiles,

590 the EOS layer reaches 100 cm, and thus the textural properties of the second layer are not available.



591 In case of the EMI-based zones (Fig. 8a-b), zone 1 is characterized by generally higher ECa_z
592 values, and identifies areas with a substantial average clay content, especially in the second soil
593 layer (18.6%). Moreover, the sandier top layer is rather shallow and starts at around 54 cm depth.
594 Moving from zone 1 to zone 4, ECa_z generally decreases. At the same time, the depth of the EOS
595 layer becomes deeper while the clay and silt content of the soil decreases and the sand content
596 increases. In zone 4, the average clay content up to 100 cm is 4.1%, while the sand content is
597 86.2%. In the case of the NDVI-based management zones (Fig. 8c-d), the three zones appear to be
598 more indicative of crop development, which results in typical soil profiles with differences that
599 seem less pronounced compared to the case of EMI-based zonation. In this case, NDVI is generally
600 higher in Cluster 1 and lowest in Cluster 3. The change in soil characteristics between zones
601 follows a similar trend compared to that of EMI-based zones. The depth of the interface between
602 soil layer 1 and 2 increases from 62.7 to 87.4 cm from zone 1 to 3, while the sand content of both
603 layers also increases (from 68.6 to 87.2 % and 58.1 to 66.1 %, respectively). The management
604 zones derived from the combined EMI-NDVI dataset (Fig. 8e-f) have typical soil profiles that are
605 similar to those based on NDVI. Also, the sand, silt, and clay content of the first soil layer appear
606 to be rather similar. However, the range of the depth of the interface between soil layer 1 and 2 is
607 higher for the EMI-NDVI clustered map (63.8 to 100 cm) compared to that of NDVI-based profiles
608 (62.7 to 87.4 cm). At the same time, the difference in texture between the second soil layer of
609 Clusters 1 and 2 is stronger in the profiles based on a combination of EMI and NDVI data (see
610 Table 3). These two factors show that the management zones from EMI and NDVI have a relatively
611 high variation between soils of different management zones, which is an improvement compared
612 to the case of the NDVI-based management zones.



613

614 Figure 8. Final management zone maps derived from (a) EMI, (c) NDVI, and (e) a combination
615 of EMI and NDVI datasets. Each zone represents areas with similar subsurface and/or above-
616 ground characteristics. (b, d, f) Corresponding soil profiles for each management zone, detailing
617 soil texture (sand-silt-clay %), dotted lines between zones indicate depth of textural change (Layer
618 1: above EOS; Layer 2: below EOS) and error bar represents the standard error. The soil profiles
619 illustrate significant variability between zones, providing critical insights for field management.

620



621 In a final step, statistical validation of the management zones was conducted using pairwise t-tests
622 to evaluate the degree of significant differences in yield and soil properties across consecutive
623 zones. The results are summarized in Table 4. A pairwise t-test for neighbouring zones derived
624 from EMI indicated that the yield of 2012, 2013, and 2016 was not significantly different between
625 zone 1 and zone 2 ($p = 0.603, 0.060, 0.253$) while the yield of 2012 was not significantly different
626 between zone 2 and 3 ($p = 0.209$). All other pairwise comparisons indicated significant differences
627 in mean yield. The textural composition of layer 1 was significantly different between all EMI-
628 derived zones. On the contrary, the depth of top layer was not significantly different between zone
629 2 and 3 ($p = 0.167$). In addition, the composition of soil layer 2 was not significantly different
630 between zone 1 and 2 (p of 0.498 for sand, 0.636 for silt, and 0.805 for clay).

631

632 The pairwise t-test for between neighbouring zones based on NDVI indicated that differences in
633 yield among all investigated years were statistically significant. On the contrary, both the depth of
634 the top layer and the composition of soil layer 2 were not significantly different between zone 1
635 and 2 (p of 0.147 for depth, 0.558 for sand, 0.986 for silt, and 0.627 for clay). These results show
636 that EMI-based zones subdivided the area in one additional class and provided a more
637 comprehensive representation of soil properties up to 100 cm compared to the NDVI-based zones
638 for the investigated field. At the same time, the NDVI-based zones offered a better representation
639 of yield from 2011 to 2019. Nonetheless, both the maps based on EMI and on NDVI offer valuable
640 information.

641

642 The pairwise t-test between neighbouring zones based on the combined EMI-NDVI dataset
643 showed that the three zones were significantly different for both yield and soil characteristics. This



644 indicates that integrating EMI and NDVI datasets allows for the delineation of zones that are robust
645 in representing both yield variability and soil heterogeneity. Moreover, a visual inspection of the
646 management zones maps of Fig.8 shows that both maps based solely on EMI or NDVI are affected
647 by West-East oriented patterns due to measurement direction for EMI and tractor lines in NDVI.
648 These features are not present in the management zone map that integrates EMI and NDVI,
649 suggesting that it also provides a representation of the field that is less affected by external factors.
650 These results underscore the added value of integrating complementary datasets to capture the full
651 spectrum of variability within the field, supporting more informed and effective precision
652 agriculture practices.

653

654

655

656

657

658

659

660

661

662



663 Table 4. Results of the pairwise t-tests for yield and soil properties between management zones
 664 derived from EMI, NDVI, and EMI-NDVI. Bold font indicates significant differences.

| | | EMI | | | NDVI | | EMI - NDVI | | |
|------------------------|------|------------------------|---------|---------|---------|---------|------------|---------|---------|
| | | Cluster | 1vs2 | 2vs3 | 3vs4 | 1vs2 | 2vs3 | 1vs2 | 2vs3 |
| Yield | | 2011 | < 0.001 | < 0.001 | < 0.001 | < 0.001 | < 0.001 | < 0.001 | < 0.001 |
| | | 2012 | 0.603 | 0.209 | < 0.001 | < 0.001 | < 0.001 | < 0.001 | < 0.001 |
| | | 2013 | 0.060 | 0.008 | < 0.001 | < 0.001 | < 0.001 | < 0.001 | < 0.001 |
| | | 2014 | < 0.001 | < 0.001 | < 0.001 | < 0.001 | < 0.001 | < 0.001 | < 0.001 |
| | | 2015 | 0.007 | < 0.001 | < 0.001 | < 0.001 | < 0.001 | < 0.001 | < 0.001 |
| | | 2016 | 0.253 | < 0.001 | < 0.001 | < 0.001 | < 0.001 | < 0.001 | < 0.001 |
| | | 2017 | < 0.001 | 0.002 | < 0.001 | < 0.001 | < 0.001 | < 0.001 | < 0.001 |
| | | 2018 | 0.039 | 0.007 | < 0.001 | < 0.001 | < 0.001 | < 0.001 | < 0.001 |
| | | 2019 | 0.002 | 0.003 | < 0.001 | < 0.001 | < 0.001 | < 0.001 | < 0.001 |
| | Soil | Layer 1 (above EOS) | Sand % | < 0.001 | 0.001 | < 0.001 | < 0.001 | < 0.001 | < 0.001 |
| Silt % | | | < 0.001 | 0.006 | < 0.001 | < 0.001 | < 0.001 | < 0.001 | < 0.001 |
| Clay % | | | < 0.001 | 0.014 | < 0.001 | < 0.001 | < 0.001 | < 0.001 | < 0.001 |
| Depth (cm) | | | 0.004 | 0.167 | NA | 0.147 | 0.004 | 0.002 | NA |
| Layer 2 (below EOS) | | Sand % | 0.498 | 0.010 | NA | 0.558 | < 0.001 | < 0.001 | NA |
| | | Silt % | 0.636 | 0.009 | NA | 0.986 | 0.004 | 0.003 | NA |
| | | Clay % | 0.805 | 0.056 | NA | 0.627 | < 0.001 | < 0.001 | NA |

665

666

667 3.5 Limitations and perspectives for future work

668 This study successfully demonstrated the integration of EMI and NDVI datasets for the delineation
 669 of management zones, but some limitations are still present and should be addressed in future
 670 research. The EMI data were collected during different campaigns under varying environmental
 671 conditions (e.g., soil temperature and moisture), and thus required z-score normalization to



672 minimize variability. While effective in this study, this approach may not fully account for certain
673 external factors such as the impact of different management practices in different parts of the field.
674 Similarly, the NDVI dataset was limited to the 2019 growing season due to the availability of
675 PlanetScope imagery, which became accessible for this field only in 2019. Furthermore, the field
676 was subdivided into smaller experimental patches after 2019, complicating data consistency for
677 subsequent years. While the 2019 dataset is representative of the investigated area, relying on a
678 single season of NDVI data may not fully capture interannual variability driven by climatic
679 conditions or crop management practices. Incorporating NDVI data from multiple years in future
680 studies would enable a more comprehensive analysis of temporal dynamics and their impact on
681 management zone delineation to capture yield and soil variability. Another limitation is the
682 distribution of soil sampling locations. Although the 160 sampling points provided valuable
683 insights, leveraging EMI-based maps to guide targeted soil sampling could improve spatial
684 representativeness. Additionally, while EMI in this study had a depth of investigation of up to 270
685 cm, soil sampling was limited to 100 cm depth, potentially missing soil heterogeneity that can
686 affect crops. Another factor was the data normalization before clustering, which was essential for
687 obtaining meaningful results in this study (see Appendix A). Without adequate scaling, one data
688 source can dominate the final product and render the other data sources less useful. This seems
689 especially important in precision agriculture applications where datasets typically originate from
690 diverse sources.

691

692 Future studies should focus on improving the temporal consistency of data collection and
693 increasing the density and depth of soil sampling. Long-term monitoring using datasets from
694 multiple years could provide insights into the temporal stability of management zones and their



695 relationship with yield. Additionally, the outputs of this study, such as detailed management zone
696 maps and soil characterization data, can be integrated into agroecosystem models to simulate and
697 predict the impact of different management strategies under future environmental and climatic
698 conditions. These models could help optimize irrigation, fertilization, and other field management
699 practices, further supporting decision-making for sustainable and resource-efficient agriculture.

700

701 **4 Conclusions**

702 This study integrated proximal soil sensing (EMI) and remote sensing (NDVI) data to delineate
703 high-resolution management zones in a 70 ha agricultural field. Self-Organizing Maps (SOM), an
704 advanced unsupervised machine learning technique, were combined with statistical validation
705 methods to identify spatial areas with similar above- and below-ground properties. Historical yield
706 maps and detailed soil information up to a depth of 100 cm were used to refine and validate the
707 clustering results, ensuring both their accuracy and practical applicability.

708

709 To address the variability introduced by environmental conditions during data collection, EMI
710 measurements from multiple campaigns were standardized using z-score normalization, ensuring
711 consistent input for further analysis of the investigated field. Similarly, NDVI data from the 2019
712 growing season were selected as they represented an uninterrupted crop cycle prior to the
713 subdivision of the investigated field in multiple patches. Before clustering, data was appropriately
714 normalized. The Multi-Cluster Average Standard Deviation (MCASD) method was applied to
715 determine the optimal number of clusters for different datasets. The optimal number of clusters
716 was determined to be five using the EM data, four for the NDVI date, and four for the combination
717 of EMI and NDVI datasets. However, statistical validation through Tukey's post-hoc analysis



718 using independent yield maps and soil samples reduced the clusters number to 4, 3, and 3,
719 respectively. This ensured that the clusters were not only computationally distinct with respect to
720 the input data, but also significantly different in terms of soil characteristics and yield data, thereby
721 increasing their practical relevance in precision agriculture. Finally, a two-tailed t-test was
722 performed to compare the effectiveness of the management zones maps obtained with EMI, NDVI,
723 and EMI-NDVI datasets.

724

725 Results showed that EMI-based management zones provided a better representation of subsurface
726 properties, particularly soil texture and the depth at which textural changes occur, which underlines
727 the utility of EMI for guiding soil management practices. In comparison, NDVI-based
728 management zones aligned more closely with topsoil characteristics and yield maps, effectively
729 capturing above-ground variability. In general, the integration of EMI and NDVI datasets provided
730 a more comprehensive representation of the spatial variability of both soil characteristics and yield,
731 resulting in management zones that linked both subsurface soil conditions and above-ground
732 vegetation performance. These combined zones effectively explained productivity patterns by
733 bridging the gap between soil properties and crop health.

734

735 The product of this study is a high-resolution management zonation map which would provide a
736 significant added value in precision and sustainable agriculture. Moreover, it can help in setting-
737 up of agroecosystem models for the simulation of crop performance and yield and in guiding future
738 soil sampling campaigns. Finally, the workflow proposed in this study can provide a robust
739 blueprint for unsupervised clustering of proximal soils sensing and remote sensing data in
740 agriculture, and future studies should explore the scalability of this methodology in different

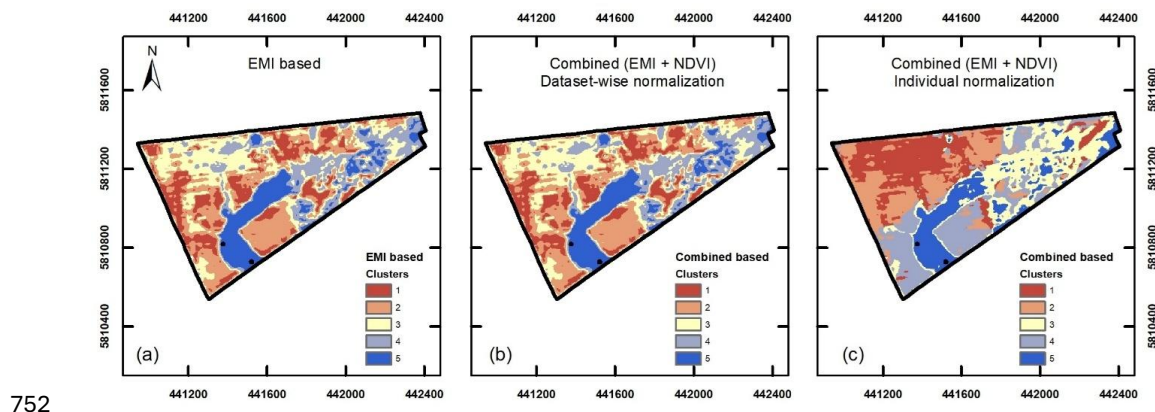


741 climatic conditions or other crop systems, as well as investigate additional data sources to further
742 enhance its representation of within-field heterogeneity in soil and crops.



743 Appendix A: Influence of data normalization

744 Figure A1 shows a visual comparison of management zone delineation using different
745 normalization approaches. These are: a) EMI-based clustering of EC_{az} maps, b) combined EMI-
746 NDVI clustering with dataset-wise normalization (i.e., normalized by using the minimum and
747 maximum values for all the available data), and c) combined EMI-NDVI clustering with dataset-
748 wise normalization of EMI data and separate column-wise normalization of NDVI data. As
749 apparent in Figure A1b, the EMI measurements dominate the clustering results when an
750 inappropriate normalization is used. On the contrary, the normalization strategy used here (Figure
751 A1c) provides a clustering result where both EMI and NDVI meaningfully contribute.



752

753 Figure A1. Comparison of management zone delineation using different normalization approaches
754 (a) EMI-based clustering without normalization, (b) Combined EMI and NDVI clustering with
755 dataset-wise normalization, (c) Combined EMI and NDVI clustering with individual
756 normalization, where EMI data were normalized as a dataset, while NDVI data were normalized
757 column-wise.

758

759



760 **Appendix B: Additional results for post-hoc analysis**

761 For the EMI dataset (VCP + HCP, 9 coils), the MCASD analysis suggested five clusters. The
 762 results of the post-hoc analysis are shown in Table B1. Statistically significant differences between
 763 two clusters are indicated by an *O* whereas an *X* indicates no significant differences. When two
 764 clusters have no statistically significant difference for any of the evaluated properties, they are
 765 merged. Therefore, clusters 4 and 5 were merged into a new cluster 4. For the NDVI dataset, the
 766 MCASD analysis suggested 4 clusters and the results of the post-hoc analysis (Table B2) merged
 767 clusters 3 and 4 into a new cluster 3. For the combined dataset (EMI + NDVI), the MCASD
 768 analysis suggested 4 clusters and the results of the post-hoc analysis (Table B3) merged clusters 1
 769 and 2 into a new cluster 1.

770

771 Table B1. Post-hoc analysis of soil characteristics and yield for the EMI-based clusters leading to
 772 cluster merging. Statistically significant (*O*) or non-significant differences (*X*) are provided
 773 between clusters for soil texture, EOS layer, and yield.

| Clusters | | 1vs2 | 2vs3 | 3vs4 | 4vs5 |
|-------------------------------|------|----------|----------|----------|----------|
| End of sandy layer (Depth cm) | | <i>O</i> | <i>X</i> | <i>O</i> | <i>X</i> |
| Layer 1 (above EOS) | Sand | <i>X</i> | <i>O</i> | <i>O</i> | <i>X</i> |
| | Silt | <i>X</i> | <i>O</i> | <i>O</i> | <i>X</i> |
| | Clay | <i>X</i> | <i>O</i> | <i>O</i> | <i>X</i> |
| Layer 2 (below EOS) | Sand | <i>X</i> | <i>X</i> | <i>O</i> | <i>X</i> |
| | Silt | <i>X</i> | <i>X</i> | <i>O</i> | <i>X</i> |
| | Clay | <i>X</i> | <i>X</i> | <i>O</i> | <i>X</i> |
| Yield | | <i>X</i> | <i>X</i> | <i>O</i> | <i>X</i> |

774



775 Table B2. Post-hoc analysis of soil characteristics and yield for the NDVI-based clusters leading
 776 to cluster merging. Statistically significant (*O*) or non-significant differences (*X*) are provided
 777 between clusters for soil texture, EOS layer, and yield.

| Clusters | | 1vs2 | 2vs3 | 3vs4 |
|-------------------------------|------|----------|----------|----------|
| End of sandy layer (depth cm) | | <i>X</i> | <i>O</i> | <i>X</i> |
| Layer 1 (above EOS) | Sand | <i>O</i> | <i>O</i> | <i>X</i> |
| | Silt | <i>O</i> | <i>O</i> | <i>X</i> |
| | Clay | <i>O</i> | <i>O</i> | <i>X</i> |
| Layer 2 (below EOS) | Sand | <i>X</i> | <i>O</i> | <i>X</i> |
| | Silt | <i>X</i> | <i>O</i> | <i>X</i> |
| | Clay | <i>X</i> | <i>O</i> | <i>X</i> |
| Yield | | <i>X</i> | <i>O</i> | <i>X</i> |

778

779 Table B3. Post-hoc analysis of soil characteristics and yield for the clusters based on EMI and
 780 NDVI leading to cluster merging. Statistically significant (*O*) or non-significant differences (*X*)
 781 are provided between clusters for soil texture, EOS layer, and yield.

| Clusters | | 1vs2 | 2vs3 | 3vs4 |
|-------------------------------|------|----------|----------|----------|
| End of sandy layer (depth cm) | | <i>X</i> | <i>O</i> | <i>O</i> |
| Layer 1 (above EOS) | Sand | <i>X</i> | <i>O</i> | <i>O</i> |
| | Silt | <i>X</i> | <i>O</i> | <i>O</i> |
| | Clay | <i>X</i> | <i>O</i> | <i>O</i> |
| Layer 2 (below EOS) | Sand | <i>X</i> | <i>O</i> | <i>X</i> |
| | Silt | <i>X</i> | <i>O</i> | <i>X</i> |
| | Clay | <i>X</i> | <i>O</i> | <i>X</i> |
| Yield | | <i>X</i> | <i>O</i> | <i>X</i> |

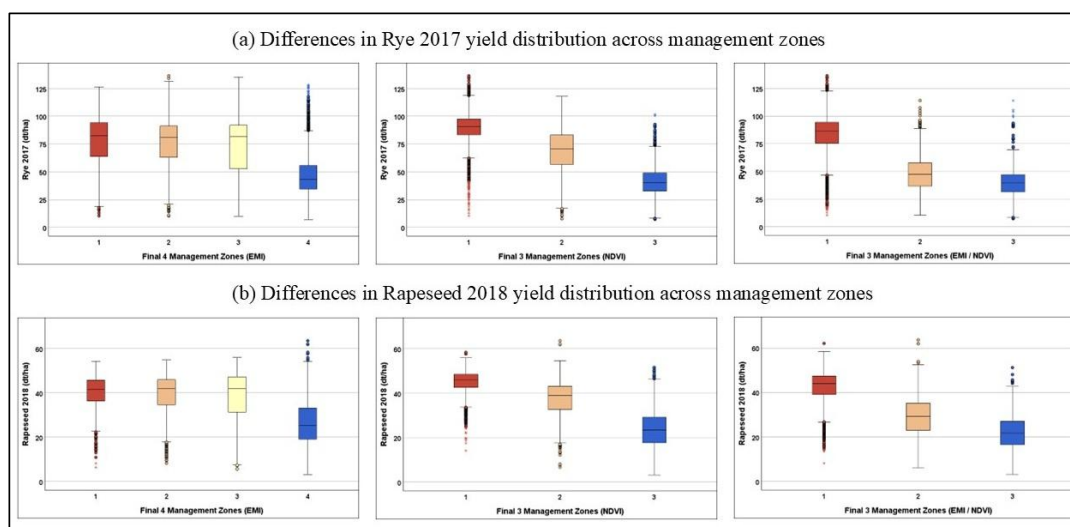
782



783 **Appendix C: Differences in yield between derived management zones for two years**

784 *Figure C1* presents boxplots illustrating yield variability (dt/ha) for Rye 2017 (Fig. C1a) and
785 Rapeseed 2018 (Fig. C1b) across management zones derived from three clustering approaches:
786 EMI-based (left), NDVI-based (middle), and combined EMI + NDVI (right). These two years were
787 selected as representative examples, as the overall yield variation across the full nine-year dataset
788 followed the same trend. In the EMI-based management zones, yield distribution is relatively
789 similar across the first three zones, with a noticeable drop in the fourth zone. In contrast, NDVI-
790 based and EMI + NDVI zones show a progressive decline in yield across clusters, indicating a
791 clearer trend of decreasing productivity.

792



793

794 *Figure C1*. Yield distribution across final management zones based on EMI, NDVI, and
795 combined EMI-NDVI datasets.

796



797 **Data availability**

798 The data that support the findings of this study are available on request from the corresponding
799 author.

800

801 **Author contributions**

802 SD, CB, and JH: conceptualization and methodology; SD, CB, MD, and IO: field measurements;
803 SD, MD, DL and CB: data analysis; SD: writing – original draft; CB, DL, IO, MD, HV, and JH:
804 writing: review and editing; JH – project supervision. All authors have read and agreed to the
805 published version of the manuscript.

806

807 **Competing interest**

808 The contact author has declared that none of the authors has any competing interests.

809

810 **Special issue statement**

811 This article is part of the special issue “Agrogeophysics: illuminating soil’s hidden dimensions”.
812 It is not associated with a conference.

813

814 **Acknowledgements**

815 We thank Kathrin Grahmann, Robert Zieciak, Anna Engels, Tawhid Hossain for local support,
816 organizational formalities and data. Danial Mansourian, Ali Chaudhry, Emilio Capitanio, Fahad
817 Muhammad, and Ali Sadrzadeh are thanked for their help during the EMI measurement campaigns.
818 The maintenance of the patchCROP infrastructure is supported by the Leibniz Centre for
819 Agricultural Landscape Research.



820

821 **Financial support**

822 This research was supported by the DFG (German Research Foundation) through the Germany's

823 Excellence Strategy EXC 2070, Grant No. 390732324 - PhenoRob.



824 **References**

- 825 Abdu, H., Robinson, D.A., Seyfried, M., Jones, S.B., 2008. Geophysical imaging of watershed
826 subsurface patterns and prediction of soil texture and water holding capacity. *Water Resour.*
827 *Res.* 44, 1–10. <https://doi.org/10.1029/2008wr007043>
- 828 Adamchuk, V., Allred, B., Doolittle, J., Grote, K., Viscarra Rossel, R.A., 2017. Tools for
829 proximal soil sensing. *Soil Surv. Man. soil Sci. Div. Staff. Washington, DC United States*
830 *Dep. Agric.* 355–356.
- 831 Adhikari, K., Smith, D.R., Collins, H., Hajda, C., Acharya, B.S., Owens, P.R., 2022. Mapping
832 Within-Field Soil Health Variations Using Apparent Electrical Conductivity, Topography,
833 and Machine Learning. *Agronomy* 12, 1–16. <https://doi.org/10.3390/agronomy12051019>
- 834 Ali, A., Rondelli, V., Martelli, R., Falsone, G., Lupia, F., Barbanti, L., 2022. Management Zones
835 Delineation through Clustering Techniques Based on Soils Traits, NDVI Data, and Multiple
836 Year Crop Yields. *Agric.* 12. <https://doi.org/10.3390/agriculture12020231>
- 837 Altdorff, D., von Hebel, C., Borchard, N., van der Kruk, J., Bogena, H.R., Vereecken, H.,
838 Huisman, J.A., 2017. Potential of catchment-wide soil water content prediction using
839 electromagnetic induction in a forest ecosystem. *Environ. Earth Sci.* 76, 1–11.
840 <https://doi.org/10.1007/s12665-016-6361-3>
- 841 Antle, J.M., Basso, B., Conant, R.T., Godfray, H.C.J., Jones, J.W., Herrero, M., Howitt, R.E.,
842 Keating, B.A., Munoz-Carpena, R., Rosenzweig, C., Tittonell, P., Wheeler, T.R., 2017.
843 Towards a new generation of agricultural system data, models and knowledge products:
844 Design and improvement. *Agric. Syst.* 155, 255–268.
845 <https://doi.org/10.1016/j.agsy.2016.10.002>
- 846 Arshad, M.A.C., Lowery, B., Grossman, B., 2015. *Physical Tests for Monitoring Soil Quality.*



- 847 pp. 123–141. <https://doi.org/10.2136/sssaspecpub49.c7>
- 848 Becker, S.M., Franz, T.E., Abimbola, O., Steele, D.D., Flores, J.P., Jia, X., Scherer, T.F.,
849 Rudnick, D.R., Neale, C.M.U., 2022. Feasibility assessment on use of proximal geophysical
850 sensors to support precision management. *Vadose Zo. J.* 21, 1–18.
851 <https://doi.org/10.1002/vzj2.20228>
- 852 Bijeesh, T. V., Narasimhamurthy, K.N., 2020. Surface water detection and delineation using
853 remote sensing images: a review of methods and algorithms. *Sustain. Water Resour. Manag.*
854 6, 1–23. <https://doi.org/10.1007/s40899-020-00425-4>
- 855 Binley, A., Hubbard, S.S., Huisman, J. a, Revil, A., Robinson, D. a, Singha, K., Slater, L.D.,
856 2015. The emergence of hydrogeophysics for improved understanding of subsurface
857 processes over multiple scales. *Water Resour. Res.* 51, 3837–3866.
858 <https://doi.org/10.1002/2015WR017016>
- 859 Blanchy, G., McLachlan, P., Mary, B., Censini, M., Boaga, J., Cassiani, G., 2024. Comparison of
860 multi-coil and multi-frequency frequency domain electromagnetic induction instruments.
861 *Front. Soil Sci.* 4, 1–13. <https://doi.org/10.3389/fsoil.2024.1239497>
- 862 Bongiovanni, R., Lowenberg-Deboer, J., 2004. Precision agriculture and sustainability. *Precis.*
863 *Agric.* 5, 359–387. <https://doi.org/10.1023/B:PRAG.0000040806.39604.aa>
- 864 Brogi, C., Huisman, J.A., Pätzold, S., von Hebel, C., Weihermüller, L., Kaufmann, M.S., van der
865 Kruk, J., Vereecken, H., 2019. Large-scale soil mapping using multi-configuration EMI and
866 supervised image classification. *Geoderma* 335, 133–148.
867 <https://doi.org/10.1016/j.geoderma.2018.08.001>
- 868 Brogi, C., Huisman, J.A., Weihermüller, L., Herbst, M., Vereecken, H., 2021. Added value of
869 geophysics-based soil mapping in agro-ecosystem simulations. *Soil* 7, 125–143.



- 870 <https://doi.org/10.5194/soil-7-125-2021>
- 871 Carfagna, E., Gallego, F.J., 2005. Using remote sensing for agricultural statistics. *Int. Stat. Rev.*
872 73, 389–404. <https://doi.org/10.1111/j.1751-5823.2005.tb00155.x>
- 873 Castrignanò, A., Buttafuoco, G., Quarto, R., Parisi, D., Viscarra Rossel, R.A., Terribile, F.,
874 Langella, G., Venezia, A., 2018. A geostatistical sensor data fusion approach for delineating
875 homogeneous management zones in Precision Agriculture. *Catena* 167, 293–304.
876 <https://doi.org/10.1016/j.catena.2018.05.011>
- 877 Celebi, M.E., Kingravi, H.A., Vela, P.A., 2013. A comparative study of efficient initialization
878 methods for the k-means clustering algorithm. *Expert Syst. Appl.* 40, 200–210.
879 <https://doi.org/10.1016/j.eswa.2012.07.021>
- 880 Chartzoulakis, K., Bertaki, M., 2015. Sustainable Water Management in Agriculture under
881 Climate Change. *Agric. Agric. Sci. Procedia* 4, 88–98.
882 <https://doi.org/10.1016/j.aaspro.2015.03.011>
- 883 Chlingaryan, A., Sukkarieh, S., Whelan, B., 2018. Machine learning approaches for crop yield
884 prediction and nitrogen status estimation in precision agriculture: A review. *Comput.*
885 *Electron. Agric.* 151, 61–69. <https://doi.org/10.1016/j.compag.2018.05.012>
- 886 Ciampalini, A., André, F., Garfagnoli, F., Grandjean, G., Lambot, S., Chiarantini, L., Moretti, S.,
887 2015. Improved estimation of soil clay content by the fusion of remote hyperspectral and
888 proximal geophysical sensing. *J. Appl. Geophys.* 116, 135–145.
889 <https://doi.org/10.1016/j.jappgeo.2015.03.009>
- 890 Corwin, D.L., Lesch, S.M., 2005. Apparent soil electrical conductivity measurements in
891 agriculture. *Comput. Electron. Agric.* 46, 11–43.
892 <https://doi.org/10.1016/j.compag.2004.10.005>



- 893 Corwin, D.L., Lesch, S.M., 2003. Application of soil electrical conductivity to precision
894 agriculture: Theory, principles, and guidelines. *Agron. J.* 95, 455–471.
895 <https://doi.org/10.2134/agronj2003.4550>
- 896 Corwin, D.L., Scudiero, E., 2019. Review of soil salinity assessment for agriculture across
897 multiple scales using proximal and/or remote sensors. *Adv. Agron.* 158, 1–130.
898 <https://doi.org/10.1016/BS.AGRON.2019.07.001>
- 899 Dobarco, M.R., McBratney, A., Minasny, B., Malone, B., 2021. A framework to assess changes
900 in soil condition and capability over large areas. *Soil Secur.* 4.
901 <https://doi.org/10.1016/j.soisec.2021.100011>
- 902 Donat, M., Geistert, J., Grahmann, K., Bloch, R., Bellingrath-Kimura, S.D., 2022. Patch
903 cropping- a new methodological approach to determine new field arrangements that
904 increase the multifunctionality of agricultural landscapes. *Comput. Electron. Agric.* 197,
905 106894. <https://doi.org/10.1016/j.compag.2022.106894>
- 906 DWD, 2021. Deutscher Wetterdienst (DWD) Climate Data Center (CDC): Monatssumme der
907 Stationsmessungen der Niederschlagshöhe in mm für Deutschland, Version v21.3,
908 Deutscher Wetterdienst.
- 909 ESRI, 2020. Esri, Maxar, Earthstar Geographics, and the GIS User Community.
- 910 Esteves, C., Fanguero, D., Braga, R.P., Martins, M., Botelho, M., Ribeiro, H., 2022. Assessing
911 the Contribution of ECa and NDVI in the Delineation of Management Zones in a Vineyard.
912 *Agronomy* 12. <https://doi.org/10.3390/agronomy12061331>
- 913 Garré, S., Hyndman, D., Mary, B., Werban, U., 2021. Geophysics conquering new territories:
914 The rise of “agrogeophysics.” *Vadose Zo. J.* 20, 2–5. <https://doi.org/10.1002/vzj2.20115>
- 915 Gebbers, R., Adamchuk, V.I., 2010. Precision Agriculture and Food Security. *Science* (80-.).



- 916 327, 828–831. <https://doi.org/10.1126/science.1183899>
- 917 Geng, X., Mu, Y., Mao, S., Ye, J., Zhu, L., 2020. An Improved K-Means Algorithm Based on
918 Fuzzy Metrics. *IEEE Access* 8, 217416–217424.
919 <https://doi.org/10.1109/ACCESS.2020.3040745>
- 920 Grahmann, K., Reckling, M., Hernández-Ochoa, I., Donat, M., Bellingrath-Kimura, S., Ewert,
921 F., 2024. Co-designing a landscape experiment to investigate diversified cropping systems.
922 *Agric. Syst.* 217. <https://doi.org/10.1016/j.agsy.2024.103950>
- 923 Grahmann, K., Reckling, M., Hernandez-Ochoa, I., Ewert, F., 2021. Intercropping for
924 sustainability: Research developments and their application An agricultural diversification
925 trial by patchy field arrangements at the landscape level: The landscape living lab
926 “patchCROP.” *Asp. Appl. Biol.* 146, 2021.
- 927 Hamidov, A., Helming, K., Bellocchi, G., Bojar, W., Dalgaard, T., Ghaley, B.B., Hoffmann, C.,
928 Holman, I., Holzkämper, A., Krzeminska, D., Kværnø, S.H., Lehtonen, H., Niedrist, G.,
929 Øygarden, L., Reidsma, P., Roggero, P.P., Rusu, T., Santos, C., Seddaiu, G., Skarbøvik, E.,
930 Ventrella, D., Żarski, J., Schönhart, M., 2018. Impacts of climate change adaptation options
931 on soil functions: A review of European case-studies. *L. Degrad. Dev.* 29, 2378–2389.
932 <https://doi.org/10.1002/ldr.3006>
- 933 Hatfield, J.L., Prueger, J.H., 2010. Value of using different vegetative indices to quantify
934 agricultural crop characteristics at different growth stages under varying management
935 practices. *Remote Sens.* 2, 562–578. <https://doi.org/10.3390/rs2020562>
- 936 Hernández-Ochoa, I.M., Gaiser, T., Grahmann, K., Engels, A., Kersebaum, K.C., Seidel, S.J.,
937 Ewert, F., 2024. Cross model validation for a diversified cropping system. *Eur. J. Agron.*
938 157. <https://doi.org/10.1016/j.eja.2024.127181>



- 939 Hou, D., Bolan, N.S., Tsang, D.C.W., Kirkham, M.B., O'Connor, D., 2020. Sustainable soil use
940 and management: An interdisciplinary and systematic approach. *Sci. Total Environ.* 729,
941 138961. <https://doi.org/10.1016/j.scitotenv.2020.138961>
- 942 Hunt, M.L., Blackburn, G.A., Carrasco, L., Redhead, J.W., Rowland, C.S., 2019. High resolution
943 wheat yield mapping using Sentinel-2. *Remote Sens. Environ.* 233, 111410.
944 <https://doi.org/10.1016/j.rse.2019.111410>
- 945 ISO, D., 2002. 11277: 2002-08. Soil Qual. Part. size Distrib. Miner. soil Mater. method by
946 sieving Sediment. <https://doi.org/10.31030/9283499>
- 947 IUSS Working Group, 2015. International soil classification system for naming soils and
948 creating legends for soil maps. *World Soil Resour. Reports* 106, 166–168.
- 949 Jadoon, K.Z., Moghadas, D., Jadoon, A., Missimer, T.M., Al-Mashharawi, S.K., McCabe, M.F.,
950 2015. Estimation of soil salinity in a drip irrigation system by using joint inversion of
951 multicoil electromagnetic induction measurements. *Water Resour. Res.* 51, 3490–3504.
952 <https://doi.org/10.1002/2014WR016245>
- 953 James, I.T., Waine, T.W., Bradley, R.I., Taylor, J.C., Godwin, R.J., 2003. Determination of Soil
954 Type Boundaries using Electromagnetic Induction Scanning Techniques. *Biosyst. Eng.* 86,
955 421–430. <https://doi.org/10.1016/j.biosystemseng.2003.09.001>
- 956 Janrao, P., Mishra, D., Bharadi, V., 2019. Clustering Approaches for Management Zone
957 Delineation in Precision Agriculture for Small Farms. *SSRN Electron. J.* 1347–1356.
958 <https://doi.org/10.2139/ssrn.3356457>
- 959 Jin, Z., Azzari, G., You, C., Di Tommaso, S., Aston, S., Burke, M., Lobell, D.B., 2019.
960 Smallholder maize area and yield mapping at national scales with Google Earth Engine.
961 *Remote Sens. Environ.* 228, 115–128. <https://doi.org/10.1016/j.rse.2019.04.016>



- 962 Kaufmann, M.S., von Hebel, C., Weihermüller, L., Baumecker, M., Döring, T., Schweitzer, K.,
963 Hobley, E., Bauke, S.L., Amelung, W., Vereecken, H., van der Kruk, J., 2020. Effect of
964 fertilizers and irrigation on multi-configuration electromagnetic induction measurements.
965 *Soil Use Manag.* 36, 104–116. <https://doi.org/10.1111/sum.12530>
- 966 Keller, G., Frischknecht, F., 1966. *Electrical Methods in Geophysical Propecting.* Oxford, New
967 York, Pergamon Press.
- 968 Khan, S., Tufail, M., Khan, M.T., Khan, Z.A., Iqbal, J., Alam, M., 2021. A novel semi-
969 supervised framework for UAV based crop/weed classification. *PLoS One* 16.
970 <https://doi.org/10.1371/journal.pone.0251008>
- 971 Kibblewhite, M.G., Ritz, K., Swift, M.J., 2008. Soil health in agricultural systems. *Philos. Trans.*
972 *R. Soc. B Biol. Sci.* 363, 685–701. <https://doi.org/10.1098/rstb.2007.2178>
- 973 Koch, T., Deumlich, D., Chiffard, P., Panten, K., Grahmann, K., 2023. Using model simulation
974 to evaluate soil loss potential in diversified agricultural landscapes. *Eur. J. Soil Sci.* 74, 1–
975 14. <https://doi.org/10.1111/ejss.13332>
- 976 Koganti, T., De Smedt, P., Farzamian, M., Knadel, M., Triantafilis, J., Christiansen, A.V., Greve,
977 M.H., 2024. Editorial: Digital soil mapping using electromagnetic sensors. *Front. Soil Sci.*
978 4, 10–12. <https://doi.org/10.3389/fsoil.2024.1536797>
- 979 Kohonen, T., 2013. Essentials of the self-organizing map. *Neural Networks* 37, 52–65.
980 <https://doi.org/10.1016/j.neunet.2012.09.018>
- 981 Kuang, B., Mahmood, H.S., Quraishi, M.Z., Hoogmoed, W.B., Mouazen, A.M., van Henten,
982 E.J., 2012. Sensing Soil Properties in the Laboratory, In Situ, and On-Line. pp. 155–223.
983 <https://doi.org/10.1016/B978-0-12-394275-3.00003-1>
- 984 Lavoué, F., Van Der Kruk, J., Rings, J., André, F., Moghadas, D., Huisman, J.A., Lambot, S.,



- 985 LWeihermüller, Vanderborcht, J., Vereecken, H., 2010. Electromagnetic induction
986 calibration using apparent electrical conductivity modelling based on electrical resistivity
987 tomography. *Near Surf. Geophys.* 8, 553–561. <https://doi.org/10.3997/1873-0604.2010037>
- 988 Li, Y., Ni, Z., Jin, F., Li, J., Li, F., 2018. Research on Clustering Method of Improved
989 Glowworm Algorithm Based on Good-Point Set. *Math. Probl. Eng.* 2018.
990 <https://doi.org/10.1155/2018/8724084>
- 991 Liaghat, S., Balasundram, S.K., 2010. A review: The role of remote sensing in precision
992 agriculture. *Am. J. Agric. Biol. Sci.* 5, 50–55. <https://doi.org/10.3844/ajabssp.2010.50.55>
- 993 Liakos, K.G., Busato, P., Moshou, D., Pearson, S., Bochtis, D., 2018. Machine learning in
994 agriculture: A review. *Sensors (Switzerland)* 18, 1–29. <https://doi.org/10.3390/s18082674>
- 995 Liang, J., Zhao, X., Li, D., Cao, F., Dang, C., 2012. Determining the number of clusters using
996 information entropy for mixed data. *Pattern Recognit.* 45, 2251–2265.
997 <https://doi.org/10.1016/j.patcog.2011.12.017>
- 998 Licker, R., Johnston, M., Foley, J.A., Barford, C., Kucharik, C.J., Monfreda, C., Ramankutty, N.,
999 2010. Mind the gap: How do climate and agricultural management explain the “yield gap”
1000 of croplands around the world? *Glob. Ecol. Biogeogr.* 19, 769–782.
1001 <https://doi.org/10.1111/j.1466-8238.2010.00563.x>
- 1002 López-Granados, F., 2011. Weed detection for site-specific weed management: mapping and
1003 real-time approaches. *Weed Res.* 51, 1–11. <https://doi.org/10.1111/j.1365-3180.2010.00829.x>
- 1004
- 1005 Lueck, E., Ruehlmann, J., 2013. Resistivity mapping with GEOPHILUS ELECTRICUS -
1006 Information about lateral and vertical soil heterogeneity. *Geoderma* 199, 2–11.
1007 <https://doi.org/10.1016/j.geoderma.2012.11.009>



- 1008 McNeill, J.D., 1980. Electromagnetic Terrain Conductivity Measurement at Low Induction
1009 Numbers.
- 1010 Meyer, S., Kling, C., Vogel, S., Schröter, I., Nagel, A., Kramer, E., Gebbers, R., Philipp, G.,
1011 Lück, K., Gerlach, F., Scheibe, D., Ruehlmann, J., 2019. Creating soil texture maps for
1012 precision liming using electrical resistivity and gamma ray mapping, in: Precision
1013 Agriculture '19. Wageningen Academic Publishers, The Netherlands, pp. 539–546.
1014 https://doi.org/10.3920/978-90-8686-888-9_67
- 1015 Mohammed, I., Marshall, M., de Bie, K., Estes, L., Nelson, A., 2020. A blended census and
1016 multiscale remote sensing approach to probabilistic cropland mapping in complex
1017 landscapes. *ISPRS J. Photogramm. Remote Sens.* 161, 233–245.
1018 <https://doi.org/10.1016/j.isprsjprs.2020.01.024>
- 1019 Moshou, D., Bravo, C., Wahlen, S., West, J., McCartney, A., De Baerdemaeker, J., Ramon, H.,
1020 2006. Simultaneous identification of plant stresses and diseases in arable crops using
1021 proximal optical sensing and self-organising maps. *Precis. Agric.* 7, 149–164.
1022 <https://doi.org/10.1007/s11119-006-9002-0>
- 1023 NRW GD, 2025. Geologischer Dienst NRW [WWW Document]. URL <https://www.gd.nrw.de/>
- 1024 O’Leary, D., Brogi, C., Brown, C., Tuohy, P., Daly, E., 2024. Linking electromagnetic induction
1025 data to soil properties at field scale aided by neural network clustering. *Front. Soil Sci.* 4, 1–
1026 13. <https://doi.org/10.3389/fsoil.2024.1346028>
- 1027 O’Leary, D., Brown, C., Healy, M.G., Regan, S., Daly, E., 2023. Observations of intra-peatland
1028 variability using multiple spatially coincident remotely sensed data sources and machine
1029 learning. *Geoderma* 430, 116348. <https://doi.org/10.1016/j.geoderma.2023.116348>
- 1030 Öttl, L.K., Wilken, F., Auerswald, K., Sommer, M., Wehrhan, M., Fiener, P., 2021. Tillage



1031 erosion as an important driver of in-field biomass patterns in an intensively used hummocky
1032 landscape. *L. Degrad. Dev.* 32, 3077–3091. <https://doi.org/10.1002/ldr.3968>
1033 patchCROP [WWW Document], 2020. URL
1034 <https://comm.zalf.de/sites/patchcrop/SitePages/Homepage.aspx>
1035 Patro, S.G.K., sahu, K.K., 2015. Normalization: A Preprocessing Stage. *Iarjset* 20–22.
1036 <https://doi.org/10.17148/iarjset.2015.2305>
1037 Pedrera-Parrilla, A., Brevik, E.C., Giráldez, J. V., Vanderlinden, K., 2016. Temporal stability of
1038 electrical conductivity in a sandy soil. *Int. Agrophysics* 30, 349–357.
1039 <https://doi.org/10.1515/intag-2016-0005>
1040 Pradipta, A., Souplos, P., Kourgialas, N., Doula, M., Dokou, Z., Makkawi, M., Alfarhan, M.,
1041 Tawabini, B., Kirmizakis, P., 2022. Precision Agriculture — Part 1 : Soil Applications.
1042 *Water* 14, 1158.
1043 Robinet, J., von Hebel, C., Govers, G., van der Kruk, J., Minella, J.P.G., Schlesner, A.,
1044 Ameijeiras-Mariño, Y., Vanderborght, J., 2018. Spatial variability of soil water content and
1045 soil electrical conductivity across scales derived from Electromagnetic Induction and Time
1046 Domain Reflectometry. *Geoderma* 314, 160–174.
1047 <https://doi.org/10.1016/j.geoderma.2017.10.045>
1048 Romero-Ruiz, A., O’Leary, D., Daly, E., Tuohy, P., Milne, A., Coleman, K., Whitmore, A.P.,
1049 2024. An agrophysical modelling framework for the detection of soil compaction spatial
1050 variability due to grazing using field-scale electromagnetic induction data. *Soil Use Manag.*
1051 40. <https://doi.org/10.1111/sum.13039>
1052 Rudolph, S., van der Kruk, J., von Hebel, C., Ali, M., Herbst, M., Montzka, C., Pätzold, S.,
1053 Robinson, D.A., Vereecken, H., Weihermüller, L., 2015. Linking satellite derived LAI



1054 patterns with subsoil heterogeneity using large-scale ground-based electromagnetic
1055 induction measurements. *Geoderma* 241–242, 262–271.
1056 <https://doi.org/10.1016/j.geoderma.2014.11.015>

1057 Saifuzzaman, M., Adamchuk, V., Buelvas, R., Biswas, A., Prasher, S., Rabe, N., Aspinall, D., Ji,
1058 W., 2019. Clustering tools for integration of satellite remote sensing imagery and proximal
1059 soil sensing data. *Remote Sens.* 11, 1–17. <https://doi.org/10.3390/rs11091036>

1060 Saputra, Danny Matthew, SAPUTRA, D., OSWARI, L.D., 2020. Effect of Distance Metrics in
1061 Determining K-Value in K-Means Clustering Using Elbow and Silhouette Method 172,
1062 341–346. <https://doi.org/10.2991/aisr.k.200424.051>

1063 Schmäck, J., Weihermüller, L., Klotzsche, A., von Hebel, C., Pätzold, S., Welp, G., Vereecken,
1064 H., 2022. Large-scale detection and quantification of harmful soil compaction in a post-
1065 mining landscape using multi-configuration electromagnetic induction. *Soil Use Manag.* 38,
1066 212–228. <https://doi.org/10.1111/sum.12763>

1067 Schubert, E., 2023. Stop using the elbow criterion for k-means and how to choose the number of
1068 clusters instead. *ACM SIGKDD Explor. Newsl.* 25, 36–42.
1069 <https://doi.org/10.1145/3606274.3606278>

1070 Simpson, D., Lehouck, A., Verdonck, L., Vermeersch, H., Van Meirvenne, M., Bourgeois, J.,
1071 Thoen, E., Docter, R., 2009. Comparison between electromagnetic induction and fluxgate
1072 gradiometer measurements on the buried remains of a 17th century castle. *J. Appl.*
1073 *Geophys.* 68, 294–300. <https://doi.org/10.1016/j.jappgeo.2009.03.006>

1074 Skakun, S., Kalecinski, N.I., Brown, M.G.L., Johnson, D.M., Vermote, E.F., Roger, J.C., Franch,
1075 B., 2021. Assessing within-field corn and soybean yield variability from worldview-3,
1076 planet, sentinel-2, and landsat 8 satellite imagery. *Remote Sens.* 13, 1–18.



- 1077 <https://doi.org/10.3390/rs13050872>
- 1078 Stamford, J.D., Vialet-Chabrand, S., Cameron, I., Lawson, T., 2023. Development of an accurate
1079 low cost NDVI imaging system for assessing plant health. *Plant Methods* 19, 1–19.
1080 <https://doi.org/10.1186/s13007-023-00981-8>
- 1081 Tagarakis, A., Liakos, V., Fountas, S., Koundouras, S., Gemtos, T.A., 2013. Management zones
1082 delineation using fuzzy clustering techniques in grapevines. *Precis. Agric.* 14, 18–39.
1083 <https://doi.org/10.1007/s11119-012-9275-4>
- 1084 Taşdemir, K., Milenov, P., Tapsall, B., 2012. A hybrid method combining SOM-based clustering
1085 and object-based analysis for identifying land in good agricultural condition. *Comput.*
1086 *Electron. Agric.* 83, 92–101. <https://doi.org/10.1016/j.compag.2012.01.017>
- 1087 Trivedi, M.B., Marshall, M., Estes, L., de Bie, C.A.J.M., Chang, L., Nelson, A., 2023. Cropland
1088 Mapping in Tropical Smallholder Systems with Seasonally Stratified Sentinel-1 and
1089 Sentinel-2 Spectral and Textural Features. *Remote Sens.* 15.
1090 <https://doi.org/10.3390/rs15123014>
- 1091 UN, 2021. Do you know all 17 SDGs? (2021) [WWW Document]. URL
1092 <https://sdgs.un.org/goals>
- 1093 Usama, M., Qadir, J., Raza, A., Arif, H., Yau, K.L.A., Elkhatib, Y., Hussain, A., Al-Fuqaha, A.,
1094 2019. Unsupervised Machine Learning for Networking: Techniques, Applications and
1095 Research Challenges. *IEEE Access* 7, 65579–65615.
1096 <https://doi.org/10.1109/ACCESS.2019.2916648>
- 1097 Valentine, A., Kalnins, L., 2016. An introduction to learning algorithms and potential
1098 applications in geomorphometry and Earth surface dynamics. *Earth Surf. Dyn.* 4, 445–460.
1099 <https://doi.org/10.5194/esurf-4-445-2016>



- 1100 Vogel, S., Gebbers, R., Oertel, M., Kramer, E., 2019. Evaluating soil-borne causes of biomass
1101 variability in Grassland by remote and proximal sensing. *Sensors (Switzerland)* 19, 1–16.
1102 <https://doi.org/10.3390/s19204593>
- 1103 von Hebel, C., Matveeva, M., Verweij, E., Rademske, P., Kaufmann, M.S., Brogi, C.,
1104 Vereecken, H., Rascher, U., van der Kruk, J., 2018. Understanding Soil and Plant
1105 Interaction by Combining Ground-Based Quantitative Electromagnetic Induction and
1106 Airborne Hyperspectral Data. *Geophys. Res. Lett.* 45, 7571–7579.
1107 <https://doi.org/10.1029/2018GL078658>
- 1108 von Hebel, C., Reynaert, S., Pauly, K., Janssens, P., Piccard, I., Vanderborght, J., van der Kruk,
1109 J., Vereecken, H., Garré, S., 2021. Toward high-resolution agronomic soil information and
1110 management zones delineated by ground-based electromagnetic induction and aerial drone
1111 data. *Vadose Zo. J.* 20, 1–18. <https://doi.org/10.1002/vzj2.20099>
- 1112 von Hebel, Christian, Rudolph, S., Mester, A., Huisman, J.A., Kumbhar, P., Vereecken, H., van
1113 der Kruk, J., 2014. Three-dimensional imaging of subsurface structural patterns using
1114 quantitative large-scale multiconfiguration electromagnetic induction data. *Water Resour.*
1115 *Res.* 50, 2732–2748. <https://doi.org/10.1002/2013WR014864>
- 1116 von Hebel, C., Rudolph, S., Mester, A., Huisman, J.A., Kumbhar, P., Vereecken, H., van der
1117 Kruk, J., 2014. *Water Resources Research* 5375–5377.
1118 <https://doi.org/10.1002/2013WR014979.Reply>
- 1119 Wang, F., Yang, S., Wei, Y., Shi, Q., Ding, J., 2021. Characterizing soil salinity at multiple
1120 depth using electromagnetic induction and remote sensing data with random forests: A case
1121 study in Tarim River Basin of southern Xinjiang, China. *Sci. Total Environ.* 754, 142030.
1122 <https://doi.org/10.1016/j.scitotenv.2020.142030>



- 1123 Wang, L., Duan, Y., Zhang, L., Rehman, T.U., Ma, D., Jin, J., 2020. Precise estimation of NDVI
1124 with a simple NIR sensitive RGB camera and machine learning methods for corn plants.
1125 Sensors (Switzerland) 20, 1–15. <https://doi.org/10.3390/s20113208>
- 1126 Ward, S.H., Hohmann, G.W., 1988. 4. Electromagnetic Theory for Geophysical Applications, in:
1127 Electromagnetic Methods in Applied Geophysics. Society of Exploration Geophysicists, pp.
1128 130–311. <https://doi.org/10.1190/1.9781560802631.ch4>
- 1129 Weiss, M., Jacob, F., Duveiller, G., 2020. Remote sensing for agricultural applications: A meta-
1130 review. Remote Sens. Environ. 236, 111402. <https://doi.org/10.1016/j.rse.2019.111402>
- 1131 Wilhelm, W.W., Ruwe, K., Schlemmer, M.R., 2000. Comparison of three leaf area index meters
1132 in a corn canopy. Crop Sci. 40, 1179–1183. <https://doi.org/10.2135/cropsci2000.4041179x>
- 1133 Xue, J., Su, B., 2017. Significant remote sensing vegetation indices: A review of developments
1134 and applications. J. Sensors 2017. <https://doi.org/10.1155/2017/1353691>
- 1135 Ylagan, S., Brye, K.R., Ashworth, A.J., Owens, P.R., Smith, H., Poncet, A.M., 2022. Using
1136 Apparent Electrical Conductivity to Delineate Field Variation in an Agroforestry System in
1137 the Ozark Highlands. Remote Sens. 14, 1–25. <https://doi.org/10.3390/rs14225777>
- 1138 Zhang, Y., Wang, Y., 2023. Machine learning applications for multi-source data of edible crops:
1139 A review of current trends and future prospects. Food Chem. X 19, 100860.
1140 <https://doi.org/10.1016/j.fochx.2023.100860>
- 1141 Zhu, Q., Lin, H., Doolittle, J., 2010. Repeated Electromagnetic Induction Surveys for
1142 Determining Subsurface Hydrologic Dynamics in an Agricultural Landscape. Soil Sci. Soc.
1143 Am. J. 74, 1750–1762. <https://doi.org/10.2136/sssaj2010.0055>
- 1144